Journal of proteome research

pubs.acs.org/jpr

Article

Open Access

This article is licensed under CC-BY 4.0

Time- and Dose-Resolved DIA-PASEF Proteomics Maps the Transition from Adaptive Stress to Apoptotic Collapse in Melittin-Treated MDA-MB-231 Cells

Farnaz Fatahian,[§] Seyed Mohammad Jafar Seyed Golestan,[§] Clizia Chinello,[*] Lisa Pagani, Hassan Rezadoost, Hossein Behboudi, Alireza Ghassempour,[*,§] and Andrew Smith[§]

Cite This: *J. Proteome Res.* 2026, 25, 4704−4718

Read Online

ACCESS | Metrics & More | Article Recommendations | Supporting Information

ABSTRACT: Melittin, the cytolytic peptide of honeybee venom, exhibits potent anticancer activity in triple-negative breast cancer (TNBC), yet the molecular programs underlying its cytotoxic effects remain incompletely defined. To address this gap, MDA-MB-231 TNBC cells were exposed to melittin at half-maximal inhibitory concentration(half IC_{50}) and IC_{50} across early(0.5, 1, and 2 h), mid(3, 4 h), and late (12, 24 h) time windows. Proteomic profiling was performed using label-free data-independent acquisition(DIA) parallel accumulation−serial fragmentation(PASEF). Approximately 5800 proteins were quantified, revealing distinct dose-dependent stress responses. An integrative exploratory framework combining time-resolved $\log_2$ fold-change trajectories, area-under-the-curve-(AUC) based temporal prioritization, and independent heatmap visualization identified proteins associated with melittin-induced stress remodeling. Half IC_{50} exposure showed a transient stress-adaptive signature characterized by chromatin remodeling(HMGN2, H2AZ1), structural and RNA-associated buffering(LRRC7), and indirect mitochondrial quality-control signaling(CPAMD8, SPATA4), which progressively weakened over time. In contrast, IC_{50} treatment induced rapid chromatin remodeling dominated by histone H1 variants(H1.4, H1.2), early RNA instability(LRRC7), and late-stage cytoskeletal disassembly marked by MICAL3 induction, consistent with progression toward apoptosis. These trajectories paralleled dose-dependent apoptotic phenotypes. Overall, data suggest that melittin elicits dose- and time-dependent proteomic stress responses in TNBC cells and identify candidate trajectory-associated proteins and pathways linked to adaptive stress remodeling or progression toward cytotoxic collapse.

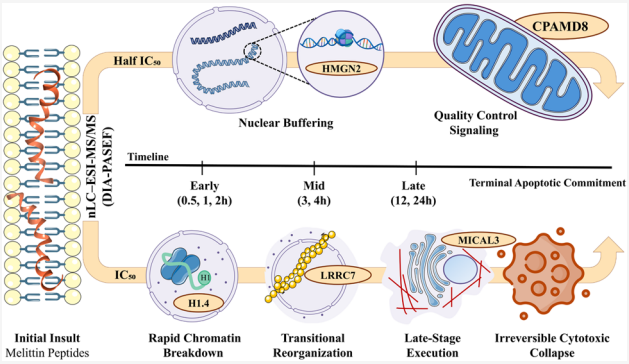

KEYWORDS: *melittin, triple-negative breast cancer, DIA-PASEF proteomics, dose-dependent stress response, chromatin remodeling, cytoskeletal disassembly, apoptosis*

1. INTRODUCTION

Breast cancer remains the most commonly diagnosed cancer in women worldwide and one of the leading causes of cancer-related mortality among women, with over 2.3 million new cases and over 670,000 deaths reported globally in 2022 according to GLOBOCAN estimates.[1−3] Recent projections indicate that the global burden of breast cancer will continue to rise substantially by 2050, particularly among younger women and in low- and middle-income countries, highlighting an urgent need for improved therapeutic strategies and earlier intervention approaches.[2,4] Within this diverse disease, triple-negative breast cancer (TNBC) is a particularly aggressive subtype, accounting for approximately 10−20% of cases and predominantly affecting younger patients.[5−7] TNBC is defined by the absence of estrogen receptor (ER), progesterone receptor (PR), and human epidermal growth factor receptor 2 (HER2) amplification and comprises distinct molecular subtypes with heterogeneous biology and therapeutic vulnerabilities.[8−10] However, the lack of approved targeted therapies for most TNBC subgroups means that systemic treatment largely relies on cytotoxic chemotherapy, sometimes combined with immune checkpoint blockade or poly(ADP-ribose) polymerase inhibition in selected patients.[11,12] Despite these advances, metastatic TNBC continues to have a poor prognosis, with five-year overall survival in the metastatic setting often below 30%, mostly due to early relapse, visceral dissemination, and rapid development of chemoresistance.[13]

Received: March 13, 2026
Revised: July 28, 2026
Accepted: July 29, 2026
Published: August 6, 2026



ACS Publications

© 2026 The Authors. Published by American Chemical Society

Downloaded from pubs.acs.org/jproteome/article-pdf/25/9/4704/6644586/acs.jproteome.6c00241.pdf by guest on 27 November 2026

This aggressive behavior is driven by adaptive mechanisms such as cell-state plasticity, metabolic reprogramming, and activation of stress-response pathways that promote survival under therapeutic pressure.[14−16] A key unresolved question is how early adaptive stress responses progressively transition into broader cytotoxic dysfunction across increasing exposure intensity and time. Understanding how these adaptive programs evolve over time and across varying drug doses is therefore essential for rational optimization of treatment strategies in this challenging subtype.

Natural products remain a valuable source of anticancer agents, and honeybee venom has attracted considerable interest due to the diverse biological activities of its principal peptide component, melittin.[17−19] Melittin is a 26-amino-acid amphipathic α-helical peptide that disrupts membrane integrity by inserting into lipid bilayers and forming transient pores, leading to mitochondrial dysfunction, endoplasmic reticulum stress, and activation of regulated cell death pathways including apoptosis and ferroptosis.[20−27] Melittin also interferes with oncogenic pathways such as nuclear factor kappa B (NF-κB), phosphoinositide 3-kinase/protein kinase B/mechanistic target of rapamycin (PI3K/AKT/mTOR), and Janus kinase/signal transducer and activator of transcription (JAK/STAT) signaling, contributing to antiproliferative and pro-apoptotic effects in cancer cells.[28−30] Preclinical studies in breast cancer models, including TNBC cell lines, have demonstrated that melittin suppresses proliferation, migration, and invasion while enhancing chemosensitivity, particularly when delivered through nanoparticles or liposomes systems designed to reduce dose-limiting toxicities such as hemolysis.[17,31] However, much of the existing literature relies on single-end point viability assays, limited biomarker panels, or targeted analyses that fail to capture the temporal and dose-dependent complexity of melittin-induced proteomic remodeling in TNBC cells.[24,32−34] Furthermore, concerns regarding systemic toxicity and peptide instability continue to limit its therapeutic development,[17] underscoring the need for dynamic mechanistic investigations that delineate how half-maximal inhibitory concentration (half IC_{50}) and IC_{50} exposure conditions differentially perturb survival and death pathways over time, rather than focusing exclusively on terminal cytotoxicity.

Mass spectrometry (MS)-based proteomics has transformed the analysis of global drug responses in cancer, enabling unbiased, large-scale measurement of protein levels and modifications with high depth and dynamic range.[35−38] Label-free quantitative proteomics is now widely applied in perturbation experiments, providing reliable relative quantification across multiple conditions without the need for isotopic labeling and allowing detection of subtle but biologically meaningful alterations in signaling and metabolic pathways.[39−41] The introduction of data-independent acquisition (DIA) workflows combined with trapped ion mobility spectrometry and parallel accumulation−serial fragmentation (PASEF) on timsTOF platforms has further improved proteome coverage, quantitative accuracy, and throughput.[42−44] These characteristics make DIA-PASEF especially suitable for time- and dose-resolved studies of drug action, where capturing coordinated changes across translation, RNA metabolism, proteostasis, and cell-death pathways requires both analytical depth and quantitative reproducibility. Meanwhile, advances in statistical and bioinformatic pipelines now enable the integration of enriched pathways such as ribosome biogenesis, mRNA surveillance, the ubiquitin−proteasome system (UPS), autophagy and mitophagy pathways, and DNA-damage responses, offering a systems-level view of cancer cell adaptation under therapeutic stress.[45−48]

Despite these methodological advances, a comprehensive DIA-PASEF-based map of the time- and dose-dependent proteomic response to melittin in TNBC remains unavailable. Previous studies in TNBC have highlighted dysregulation of translation machinery, ribosome biogenesis, and RNA-processing pathways as key features that support rapid cell growth and contribute to therapeutic resistance.[49] Similarly, abnormal RNA splicing and mRNA surveillance have been linked to the production of oncogenic isoforms and to buffering stress signals, thus supporting survival during cytotoxic treatments.[50,51] Proteostasis networks, including the UPS, endoplasmic reticulum stress response, and autophagy, are also essential for maintaining protein homeostasis in TNBC and can shift the outcome toward survival or cell death when overwhelmed.[52,53] Melittin, by simultaneously disrupting plasma membrane integrity, mitochondrial function, and endoplasmic reticulum homeostasis, is positioned to affect many of these pathways. However, the sequence of events from early adaptive responses at half IC_{50} doses to widespread perturbation of RNA−protein homeostasis and activation of cell-death mechanisms at IC_{50} doses has not been mapped in a time-resolved, systems-level manner in TNBC cells. Therefore, this study aimed to apply DIA-PASEF proteomics to investigate time- and dose-dependent proteomic responses to melittin in MDA-MB-231 human TNBC cells with particular focus on the temporal transition from adaptive stress remodeling to progressive cytotoxic dysfunction.

2. MATERIALS AND METHODS

2.1. Reagents and Materials

RPMI-1640 cell culture medium, fetal bovine serum (FBS), and penicillin-streptomycin were purchased from Gibco (Paisley, U.K.). 3-(4,5-dimethylthiazol-2-yl)-2,5-diphenyltetrazolium bromide (MTT) reagent, dimethyl sulfoxide (DMSO), and phosphate-buffered saline (PBS) were obtained from Sigma-Aldrich (Burlington, Switzerland). The melittin used in this study was purified to >98% purity using our previously published RP−HPLC workflow.[54] Additional reagents included RapiGest SF surfactant (Waters, Milford, MA, USA), DL-dithiothreitol (DTT), iodoacetamide (IAA), sequencing-grade trypsin from porcine pancreas (all from Sigma-Aldrich), trifluoroacetic acid (TFA; Honeywell SC, Seelze, Germany), citric acid and ammonium bicarbonate (NH_4HCO_3; Sigma-Aldrich). LC−MS grade water, acetonitrile (ACN), and formic acid (FA) were obtained from Merck KGaA (Darmstadt, Germany) and used as mobile-phase solvents. Pierce HeLa Protein Digest Standard (Thermo Scientific, Waltham, MA, USA) and MMI-L low concentration tuning mix (Agilent Technologies, Santa Clara, CA, USA) were employed for quality control and instrument calibration. Acridine orange (AO) and ethidium bromide (EB) (Sigma-Aldrich) were used for fluorescence microscopy.

2.2. Cell Culture and IC_{50} Determination

MDA-MB-231 cell line (Pasteur Institute, Tehran, Iran) was cultured in RPMI-1640 medium supplemented with 10% FBS and 1% penicillin−streptomycin at 37 °C in a humidified incubator with 5% CO_2. For IC_{50} determination, cells were seeded at 1.5×10^4 cells per well in 96-well plates and treated with melittin (0.5−8 μg/mL) for 24 h. Cell viability was assessed using the MTT assay. After incubation with 10 μL of MTT (5 mg/mL) for 4 h, formazan crystals were dissolved in DMSO, and absorbance was measured at 570 nm. Nonlinear regression of the dose−response curve yielded an IC_{50} of 2.86 μg/mL (~1.00 μM). This concentration and its corresponding

Downloaded from pubs.acs.org/jproobs/article-pdf/25/9/4704/6645868/acs.jproteome.6c00241.pdf by guest on 27 November 2026

https://doi.org/10.1021/acs.jproteome.6c00241
J. Proteome Res. 2026, 25, 4704−4718

half IC_{50} (1.43 μg/mL; 0.50 μM) were selected for all subsequent proteomic experiments.

2.3. Melittin Treatment

MDA-MB-231 cells were treated with melittin at half IC_{50} and IC_{50} concentrations for 0.5, 1, 2, 3, 4, 12, and 24 h. Time points were grouped as early (0.5, 1, and 2 h), mid (3, 4 h), and late (12, 24 h). At each time point, culture media containing detached cells were retained to minimize the loss of apoptotic cell populations prior to sample collection. The remaining adherent cells were then washed twice with PBS and collected together with the retained cell fraction before fixation in 4% paraformaldehyde for 15 min at room temperature. Fixed pellets were stored in PBS at 4 °C until processing. A single untreated control sample was processed under the same experimental workflow and used as the common reference condition for calculations across all treatment groups and time points. Although minor differences related to culture duration or cell confluence cannot be fully excluded, all samples were handled using consistent culture and processing conditions to minimize technical variability. In total, 14 melittin-treated samples (2 doses × 7 time points) and 1 untreated control were collected for downstream proteomic analysis. For each biological condition (14 treatments +1 control), the resulting sample was injected in nano liquid chromatography−tandem mass spectrometry (nLC−MS/MS) in triplicate (n = 3), and intensities of the technical replicates for each sample were averaged for downstream analyses. No independent biological replicates were available.

2.4. Sample Preparation for nLC−MS/MS Analysis

Protein extraction and digestion followed an optimized workflow.[55] Fixed cells (~7×10^6 per sample) were pelleted (1400 rpm, 5 min, 21 °C), washed with PBS, and subjected to antigen retrieval in 10 mM citrate acid buffer (pH 6) at 97 °C for 45 min. Pellets were washed again, resuspended in 50 mM ammonium bicarbonate, and RapiGest surfactant (final 0.1%) was added to enhance protein solubilization and digestion, followed by incubation at 60 °C for 15 min. Reduction was performed with 10 mM DTT (56 °C for 45 min), and alkylation with 15 mM IAA for 30 min. Digestion proceeded overnight at 37 °C with trypsin (5 μg per sample). Reactions were quenched by acidification with TFA (final 0.5%), and precipitated surfactant was removed through centrifugation (13,000 rpm, 10 min) after an incubation of 30 min at 37 °C. Peptide solutions were dried in a centrifugal evaporator (Hetovac, Savant) and reconstituted in mobile phase A (0.1% FA in water). Peptide concentration was measured using a Nanodrop spectrophotometer (Thermo Scientific, Sunnyvale, CA) and normalized to 500 ng per injection. Each condition was analyzed with three technical replicates.

2.5. nLC−ESI-MS/MS (DIA-PASEF) Analysis

Peptides (500 ng) were analyzed using a timsTOF fleX mass spectrometer (Bruker Daltonics, Bremen, Germany) equipped with a CaptiveSpray nano-ESI source, connected to a Dionex UltiMate 3000 RSLC nano system (Thermo Scientific). Peptide separation was conducted on a 50 cm Acclaim PepMap RSLC C18 column (75 μm ID, 2 μm particle size) with a 90 min gradient from 4 to 98% mobile phase B (80% ACN/0.08% FA in water). The mass spectrometer operated in DIA-PASEF mode, following parameters adapted from recent publications.[56,57] Ion samples were analyzed in positive polarity across an m/z range of 100−1700 and a mobility range of 0.60−1.60 V·s/cm^2. The dry gas flow was set to 3.0 L/min at 180 °C, and the capillary voltage was 1650 V. For tandem mass PASEF analysis, singly charged ion clusters were excluded to decrease MS/MS spectra complexity, using the parameters m/z 300−1201 Da and mobility range 0.60−1.43 V·s/cm^2. The estimated cycle time for each PASEF acquisition was 1.80 s, with a total of 36 cycles using DIA windows of 25 Da. The mass spectrometer was calibrated for both mass and ion mobility accuracy with a mixture of ten known standards (MMI-L Low Concentration Tuning Mix). For nanosource calibration, three lock masses (622.0290, 922.0098, and 1221.9906 m/z) were used through a dedicated filter. To minimize potential technical variability, all samples were prepared using the same workflow and analyzed within a single analytical batch under consistent instrumental conditions.

2.6. Data Processing

Raw data were elaborated by using Spectronaut (v.19.7, https://biognosys.com) following a library-free workflow. A human database (Swissprot, downloaded on 20 September 2024) was used. The parameters were set as follows: trypsin as the enzyme, carbamidomethyl (C) as the fixed modifications, acetylation (protein N-term), FFPE + 12, FFPE + 30 and oxidation (M) as the variable modifications, 1% false discovery rate (FDR) at precursor and protein levels. Abundance values were automatically normalized across runs. Proteins were considered identified and quantified only if they had at least one and two significant peptides, respectively.

2.7. Statistical and Temporal Analysis

Protein abundances were averaged across three technical replicates to produce a single quantitative value for each biological condition. Since biological replicates were unavailable, downstream analysis employed an effect size−based exploratory approach rather than traditional hypothesis testing (e.g., t tests, ANOVA, or adjusted p-values).[58,59] All subsequent analyses were performed in R (v4.5.2; The R Foundation for Statistical Computing, Vienna, Austria) and MetaboAnalyst (v5.0; McGill University, Montreal, QC, Canada). Protein intensities were $\log_2$-transformed, and $\log_2$ fold-change ($\log_2$FC) values were computed relative to the untreated control at each time point and dose (half IC_{50} and IC_{50}). Proteins were categorized as differentially expressed (DE) when $|\log_2 FC| \geq 0.58$ (approximately 1.5-fold), a threshold commonly applied in label-free DIA proteomics.[60]

To summarize temporal proteomic behavior, proteins were grouped into three biological windows: early (0.5, 1, and 2 h), mid (3, 4 h), and late (12, 24 h). For each protein and dose condition, $\log_2$ FC values relative to untreated controls were integrated within each temporal window using trapezoidal area under the curve (AUC) integration based on the actual experimental time intervals.[61] Because both sustained upregulation and sustained downregulation may reflect biologically relevant perturbation, absolute AUC values were used for ranking purposes. An exploratory trajectory rank score was therefore calculated as Rank = $|AUC_{early}| + 0.5|AUC_{mid}| + 0.5|AUC_{late}|$. A schematic overview of the trajectory score calculation workflow, temporal windowing strategy, and trapezoidal AUC integration is provided in Figure S1. This weighting scheme was designed to prioritize proteins exhibiting strong early temporal perturbations while still incorporating sustained mid- and late-stage remodeling. Importantly, this exploratory score reflects the cumulative magnitude of temporal proteomic deviation rather than the direction of regulation. Consequently, proteins showing biphasic or direction-switching behavior may also achieve high trajectory scores. The ranking strategy was therefore used solely for descriptive prioritization and visualization of strongly perturbed temporal profiles rather than inferential statistical analysis. Separately, heatmap visualization was generated using proteins ranked by the cumulative absolute $\log_2$FC magnitude across all measured time points rather than by AUC-derived trajectory scores. To further examine directional temporal behavior, Venn diagrams for up and down-regulated proteins across early, mid, and late windows, as well as across doses, were generated using the ggVennDiagram package in R. Bar plots of DE protein counts (Up/Down × dose × time) were created with ggplot2. Exploratory multivariate analyses, including principal component analysis (PCA), were used for pattern discovery and visualization rather than hypothesis testing. PCA was performed in MetaboAnalyst, with samples represented as separate technical replicates solely for visualization. Because no formal clustering analysis was performed, PCA results were interpreted qualitatively, and no statistical inference was drawn from these PCA plots.

2.8. Functional Enrichment Analysis

Significant protein lists (separately for half IC_{50} and IC_{50}) were analyzed in g:Profiler (https://biit.cs.ut.ee/gprofiler/gost) for GO terms (BP, CC, MF). Enriched terms with FDR ≤ 0.05 were retained.

Downloaded from pubs.acs.org/jproteome/article-pdf/25/9/4704/6645868/acs.jproteome.6c00241.pdf by guest on 27 November 2026

https://doi.org/10.1021/acs.jproteome.6c00241
J. Proteome Res. 2026, 25, 4704−4718

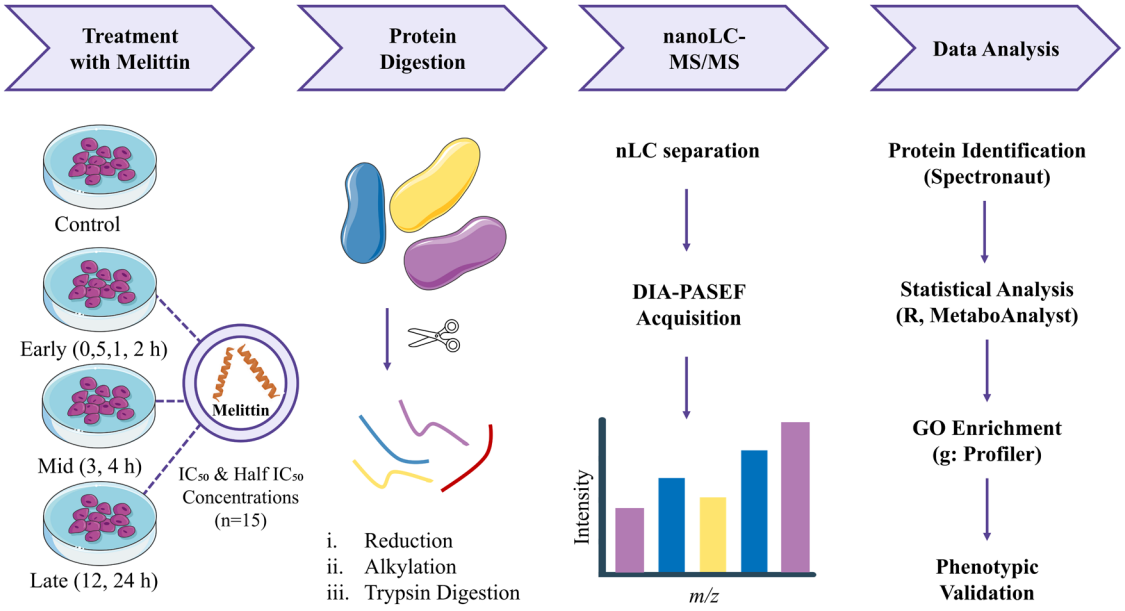

Figure 1. Experimental design and DIA-PASEF proteomics workflow. MDA-MB-231 TNBC cells were treated with melittin at half IC_{50} (1.43 μg/mL) and IC_{50} (2.86 μg/mL) across seven time points (0.5, 1, 2, 3, 4, 12, and 24 h), grouped into early (0.5, 1, and 2 h), mid (3, 4 h), and late (12, 24 h) phases, followed by protein extraction, reduction, alkylation, tryptic digestion, nLC separation, and DIA-PASEF analysis using a timsTOF fleX mass spectrometer. Protein identification, label-free quantification, and downstream pathway enrichment analyses were subsequently performed. In total, 15 biological conditions were analyzed (14 treated groups and 1 untreated control), each acquired in three technical replicate nLC−MS/MS injections (n = 3).

To reduce redundancy, terms were manually consolidated by gene ontology (GO) hierarchy and gene overlap.

2.9. Flow Cytometry Analysis of Apoptosis and Necrosis by Annexin V−FITC/PI Staining

Apoptotic and necrotic cell death induced by melittin using an Annexin V−FITC/propidium iodide (PI) apoptosis detection kit (BioLegend, Cat. No. 640914), following the manufacturer's protocol with optimized titration-based staining conditions.[62] MDA-MB-231 cells were seeded in 6-well plates at 2×10^5 cells per well and allowed to adhere overnight. Cells were treated with melittin at the IC_{50} concentration (2.86 μg/mL) for 1, 4, 12, and 24 h, alongside an untreated control. After treatment, cells were gently trypsinized, washed twice with ice-cold PBS (at 1500 rpm for 5 min), and resuspended in 500 μL of 1× Binding Buffer. To establish compensation and correct for spectral overlap between FITC and PI, each sample was divided into four tubes: (1) unstained cells, (2) cells stained only with Annexin V−FITC, (3) cells stained only with PI, and (4) cells stained with both Annexin V−FITC and PI (test sample). For staining, 3 μL of Annexin V−FITC was added to tubes #2 and #4, followed by a 15 min incubation at room temperature in the dark. Then, samples were washed once with Binding Buffer, centrifuged at 1500 rpm for 5 min, and resuspended in 500 μL of Binding Buffer. Just before flow cytometry analysis, 3 μL of PI solution was added to tubes #3 and #4. Flow cytometry was performed on a BD FACSCalibur (BD Biosciences, USA). FITC fluorescence was detected at 488/530 nm, and PI fluorescence at 535/617 nm. Compensation matrices were used to correct spectral spillover. Data analysis and quadrant gating were performed with FlowJo v10.10 software to identify cell populations: Annexin V^-/PI^- as viable cells, Annexin V^+/PI^- as early apoptotic cells, Annexin V^+/PI^+ as late apoptotic cells, and Annexin V^-/PI^+ as necrotic cells.

2.10. Fluorescent Microscopy (AO/EB Staining)

AO/EB dual fluorescent staining was performed to visually assess melittin-induced morphological features of viability, apoptosis, and necrosis in MDA-MB-231 cells. Cells were seeded into 6-well plates at a density of 2×10^5 cells per well and allowed to adhere overnight. Melittin treatment was carried out using half IC_{50} and IC_{50} concentrations for 24 h, along with an untreated control. After treatment, cells were gently washed twice with PBS and stained with an AO/EB working solution prepared by mixing AO and EB at 1 μg/mL each. A total volume of 20−25 μL of staining solution was added to each well, and the cells were immediately examined under a fluorescence microscope (Axioskop 2 Plus, Zeiss, Germany). AO selectively stains cells with intact membranes, producing green fluorescence in viable nuclei. EB penetrates only cells with compromised membranes, resulting in orange/red fluorescence in apoptotic and necrotic nuclei.

3. RESULTS AND DISCUSSION

To characterize how melittin perturbs the TNBC proteome over time, we used a combined time- and dose-resolved DIA-PASEF nLC−MS/MS workflow (Figure 1). MDA-MB-231 cells were exposed to melittin at half IC_{50} (1.43 μg/mL) and IC_{50} (2.86 μg/mL), and collected across three distinct temporal windows: early (0.5, 1, and 2 h), mid (3, 4 h), and late (12, 24 h). Tryptic peptides were analyzed on a timsTOF fleX platform, and protein-level $\log_2$FC were calculated relative to untreated controls. These changes were integrated using differential-abundance profiling, exploratory trajectory-based AUC prioritization, independent heatmap visualization of high-magnitude responders, and pathway enrichment analysis, enabling us to identify coordinated shifts in stress-response, metabolic, and cell-death programs. This experimental design offers a systems-level perspective of time- and dose-dependent proteomic changes, providing an exploratory view of how early adaptive stress responses evolve into irreversible apoptotic and metabolic collapse depending on the dose.

3.1. Effect of Melittin on TNBC Cell Viability

Treatment of MDA-MB-231 cells with increasing concentrations of melittin (0.5−8 μg/mL) for 24 h resulted in a dose-dependent decrease in cell viability, as measured by the MTT assay (Figure 2).

Downloaded from pubs.acs.org/jproteome/article-pdf/25/9/4704/6645868/acs.jproteome.6c00241.pdf by guest on 27 November 2026

https://doi.org/10.1021/acs.jproteome.6c00241
J. Proteome Res. 2026, 25, 4704−4718

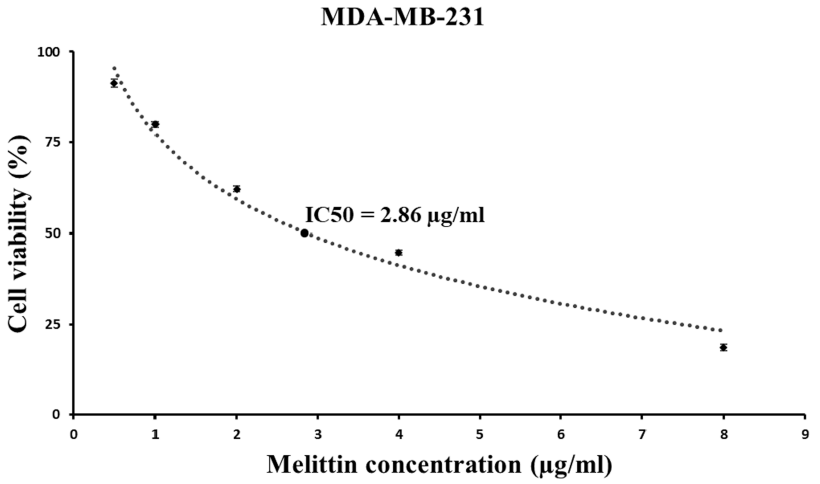

Figure 2. Dose−response curve of MDA-MB-231 cells treated with melittin for 24 h. Cell viability was measured using the MTT assay, which assesses mitochondrial metabolic activity as an indicator of viable cells. A clear dose-dependent decline in cell viability was observed following melittin treatment, and nonlinear regression analysis yielded an IC_{50} value of 2.86 μg/mL. Data presented as mean ± SD from three technical replicates (n = 3).

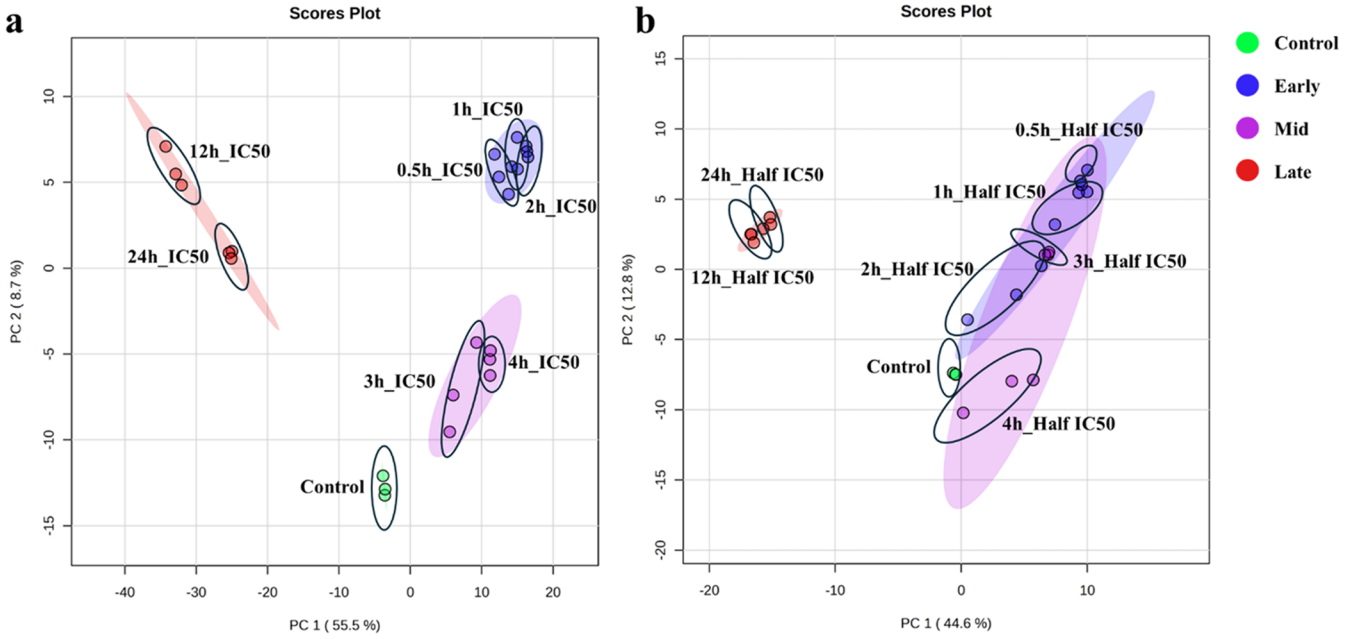

Figure 3. PCA of melittin-treated MDA-MB-231 proteomes. Scores plots showing global proteomic variation for (a) IC_{50} and (b) half IC_{50} melittin treatments across all time points. Each point represents one technical nLC-MS/MS injection, and colors indicate temporal phases: early (0.5−2 h), mid (3−4 h), late (12−24 h), and untreated control samples (green). Progressive separation of treated samples from controls reflects time- and dose-dependent proteome remodeling, with half IC_{50} samples remaining closer to baseline than IC_{50}-treated samples. PCA was used for exploratory visualization of sample relationships and not for statistical inference.

A marked decline in survival was observed at concentrations above 2 μg/mL, indicating the high susceptibility of MDA-MB-231 cells to melittin. Nonlinear regression of the dose−response curve yielded an IC_{50} of 2.86 μg/mL (~1.0 μM), consistent with previous reports of melittin cytolytic activity in breast cancer models.[63] This IC_{50} value and the corresponding half IC_{50} concentration were used for all downstream time-resolved proteomic analyses and phenotypic validation assays.

3.2. Proteomics Overview

Label-free DIA-PASEF proteomics offered a time-resolved view of the proteomic changes in MDA-MB-231 cells in response to melittin. After stringent peptide-quality filtering and 1% FDR threshold, about 5800 proteins were confidently identified across the data set, independently of differential expression filtering, providing comprehensive coverage of the TNBC proteome. Across the 45 DIA-PASEF acquisitions, an average of ~5200 ± 200 proteins were identified per nLC−MS/MS run (range: ~4800−5500), demonstrating both the depth and consistency of the measurements. A detailed summary of protein identification and quantification metrics for each run is provided in Table S1. Protein intensities from three technical replicates per condition were averaged, log_2-transformed, and represented as log_2FC relative to the untreated control. Given the study design, downstream analyses relied solely on effect sizes (log_2FC and trajectory metrics) without formal statistical testing; exploratory multi-

https://doi.org/10.1021/acs.jproteome.6c00241
J. Proteome Res. 2026, 25, 4704−4718

Downloaded from pubs.acs.org/jproteome/article-pdf/25/9/4704/6445868/acs.jproteome.6c00241.pdf by guest on 27 November 2026

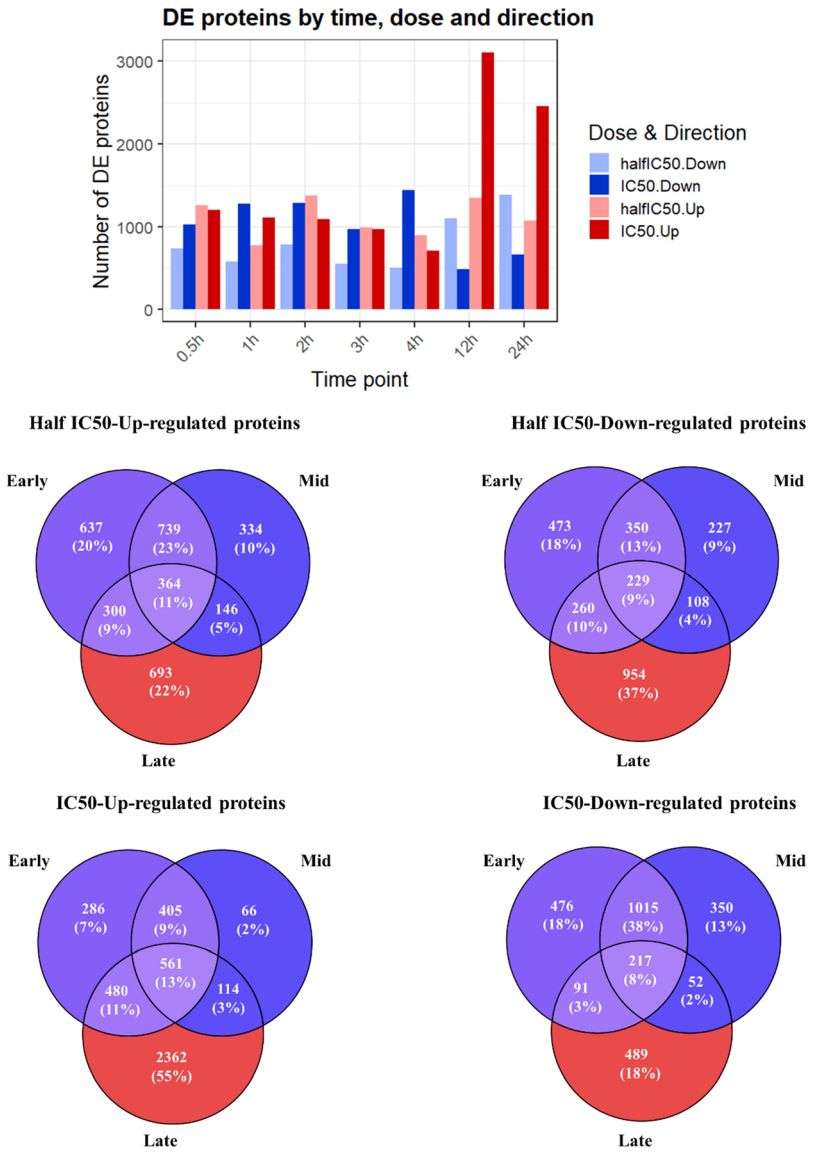

Figure 4. DE proteins following melittin exposure. (a) Time- and dose-resolved numbers of up-regulated and down-regulated proteins identified using a $|\log_2 FC| \geq 0.58$ (equivalent to ≥1.5-fold change). (b) Corresponding Venn diagrams showing overlap of DE proteins among early, mid, and late phases for half IC_{50} treatment. (c) Corresponding diagrams for IC_{50} treatment. Overlapping regions illustrate proteins shared across multiple temporal phases, whereas unique regions represent time-specific proteomic responses. The results demonstrate progressive divergence of proteomic responses over time, particularly under IC_{50} treatment.

variate plots were used only for visualization. To gain an overview of global proteomic variation, unsupervised PCA was performed using individual technical replicates (Figure 3). Under IC_{50} treatment (Figure 3a), early (0.5, 1, and 2 h), mid (3, 4 h), and late (12, 24 h) samples occupied three distinct regions of the PCA space, indicating a rapid early perturbation, a transitional intermediate phase, and significant late-stage proteome remodeling. The half IC_{50} response (Figure 3b) followed a similar temporal pattern but remained consistently closer to the control sample, aligned along PC1 and PC2, reflecting a dose-dependent attenuation and delay of the same underlying biological process. Technical replicates showed close spatial proximity within each condition in the PCA score plots, suggesting good analytical consistency of the DIA-PASEF workflow. Because PCA reflects only the major sources of variance represented by PC1 and PC2, and no formal clustering analysis was performed, these observations are interpreted qualitatively and are not used for statistical inference.

Differential expression was assessed using an effect-size threshold of $|\log_2 FC| \geq 0.58$ (about 1.5-fold), allowing for a structured, time-resolved analysis of the proteomic response to melittin. Across both doses, the number of DE proteins increased steadily from early (0.5, 1, and 2 h) to mid (3, 4 h) and late (12, 24 h) periods (Figure 4a), indicating an expansion from an initial stress response to broader, system-level disruptions. As expected due to its higher cytotoxicity, the IC_{50} dose resulted in a higher number of DE protein counts than the half IC_{50} dose, especially at later time points, reflecting a more extensive and faster breakdown of proteome homeostasis.

Venn diagram analysis showed that each temporal window contained both shared and unique DE proteins (Figure 4b,c). During early phase DE proteins demonstrated significant

https://doi.org/10.1021/acs.jproteome.6c00241
J. Proteome Res. 2026, 25, 4704−4718

Downloaded from pubs.acs.org/jproobs/article-pdf/25/9/4704/6445868/acs.jproteome.6c00241.pdf by guest on 27 November 2026

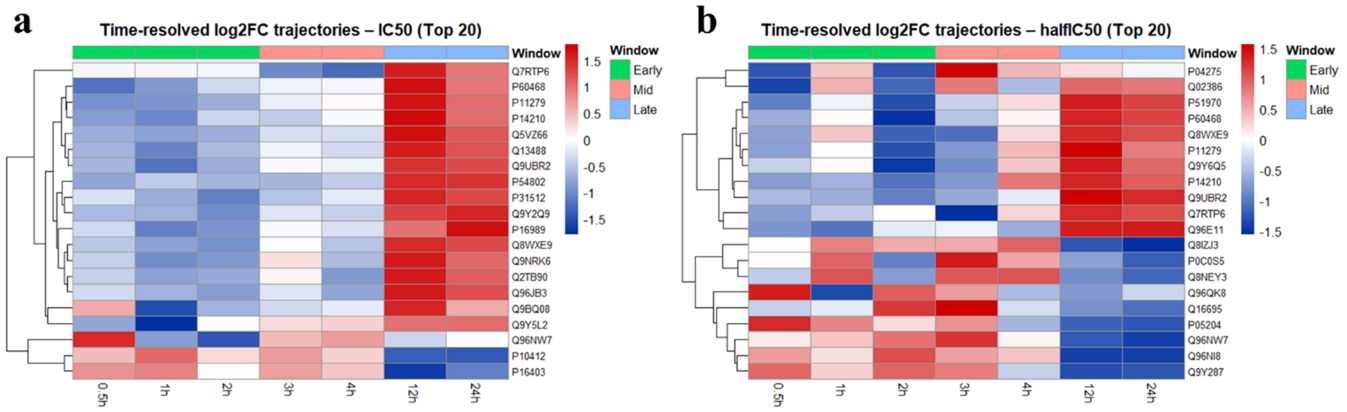

Figure 5. Heatmap showing log_2FC trajectories of the top 20 proteins selected based on cumulative absolute log_2FC magnitude across all time points under (a) IC_{50} and (b) half IC_{50} treatment. Rows represent proteins and columns represent time points spanning the early, mid, and late (0.5−24 h). Color intensity indicates relative protein abundance compared with untreated control samples (blue, down-regulation; red, up-regulation). IC_{50} treatment induced rapid and high-amplitude proteomic changes, whereas half IC_{50} elicits a more gradual and lower-magnitude adaptive response.

overlap across time points for both doses, indicating a common set of core proteins that respond immediately to melittin exposure. Specifically, the core group of proteins shared across all three-time phases (early, mid, and late) accounted for 11% (up) and 9% (down) at the half IC_{50} dose, and 13% (up) and 8% (down) at the IC_{50} dose. The overlap between the early and midphases was particularly prominent for down-regulated proteins under IC_{50} treatment, reaching 38%. The intersections during the midphase were generally smaller and more dose-dependent; unique proteins in this window made up 10% (up) and 9% (down) for half IC_{50}, compared to just 2% (up) and 13% (down) for IC_{50}. This suggests that stress-response mechanisms diversify as cells shift from adaptive signaling toward preapoptotic states. The late window had the highest number of stage-specific DE proteins, especially under IC_{50} treatment where 55% of up-regulated proteins (2362 proteins) were unique to this time point. At the half IC_{50} dose, unique late-stage proteins comprised 22% (up) and 37% (down) of the total DE counts. These findings are consistent with a widespread perturbation of RNA metabolism, translation machinery, chromatin regulation, and mitochondrial function during the later stages of melittin-induced cytotoxicity.

These DE protein trajectories closely align with the functional enrichment patterns described in Section 3.3. The shared early phase DE proteins indicate broad activation of translation, rRNA processing, and ubiquitin-dependent proteostasis pathways. Divergence during the midphase mirrors dose-dependent amplification of endoplasmic reticulum stress, RNA catabolism, and chromatin remodeling. The large late IC_{50} specific sector (55% of up-regulation) corresponds to strong enrichment of spliceosome disruption, RNA decay, ribosomal failure, and mitochondrial dysfunction. Overall, the DE protein landscape and enrichment signatures support a coherent model that is both time- and dose-dependent, wherein melittin triggers (i) a rapid, conserved stress response, followed by (ii) a transitional midphase reorganization, and at higher doses (iii) a late disruption of biosynthetic and homeostatic processes.

To understand the temporal structure of melittin-induced proteome changes, we summarized each protein's log_2FC trajectory using window-specific AUC metrics. For each protein, log_2FC values were combined across the early (0.5, 1, and 2 h), mid (3, 4 h), and late (12, 24 h) time points to generate three window-specific AUC scores. Full ranked protein lists are available in Tables S3−S4. This approach highlighted proteins involved in ER and oxidative stress, proteasomal activity, mitochondrial quality control, cytoskeletal remodeling, and apoptosis, many of which showed monotonic increases or decreases or biphasic patterns characteristic of early stress response followed by later execution phases. Complementary heatmaps of the top 20 proteins showing the largest cumulative absolute log_2FC changes across all time points illustrate the overall structure of melittin-induced temporal dynamics (Figure 5 and Tables S11−S12). Under IC_{50} concentration treatment (Figure 5a), log_2FC trajectories diverged from control early on and intensified through mid and late stages, indicating a swift transition into a strongly perturbed proteome state. In contrast, half IC_{50} exposure (Figure 5b) showed similar temporal patterns but with more gradual and lower-amplitude changes, consistent with a slower progression through the same overall response. Despite these shared temporal patterns, the underlying protein identities and associated functional annotations differed between doses, consistent with enrichment analyses suggesting that half IC_{50} mainly engages adaptive stress responses, whereas IC_{50} exposure is associated with earlier disruption of translational and RNA-processing systems. Notably, several proteins appeared in both the AUC-top20 and heatmap-top20 lists, including Q96NW7 (LRRC7), P05204 (HMGN2), Q8IZJ3 (CPAMD8), P0C0S5 (H2AZ1), and Q8NEY3 (SPATA4) under half IC_{50}, as well as P10412 (Histone H1.4), Q96NW7 (LRRC7), P16403 (Histone H1.2), and Q7RTP6 (MICAL3) under IC_{50}. This overlap suggests that these proteins exhibit both strong cumulative temporal perturbation and pronounced time-dependent expression remodeling across multiple analytical representations. Mechanistically, these candidates are biologically coherent. Histone H1.4 and H2A.Z (H2AZ1) are chromatin-associated proteins whose levels and distribution change dynamically during severe cellular stress, indicating chromatin reorganization and nuclear alteration during apoptotic progression.[64] Histone H1.2 is a linker histone that controls chromatin compaction and nuclear structure and is actively redistributed during cellular stress, where it engages in DNA damage responses and apoptosis-related chromatin remodeling.[65] HMGN2 is a nonhistone chromatin architectural protein that influences nucleosome organization, indicating chromatin remodeling and transcrip-

Downloaded from pubs.acs.org/jproteome/article-pdf/25/9/4704/6645868/acs.jproteome.6c00241.pdf by guest on 27 November 2026

https://doi.org/10.1021/acs.jproteome.6c00241
J. Proteome Res. 2026, 25, 4704−4718

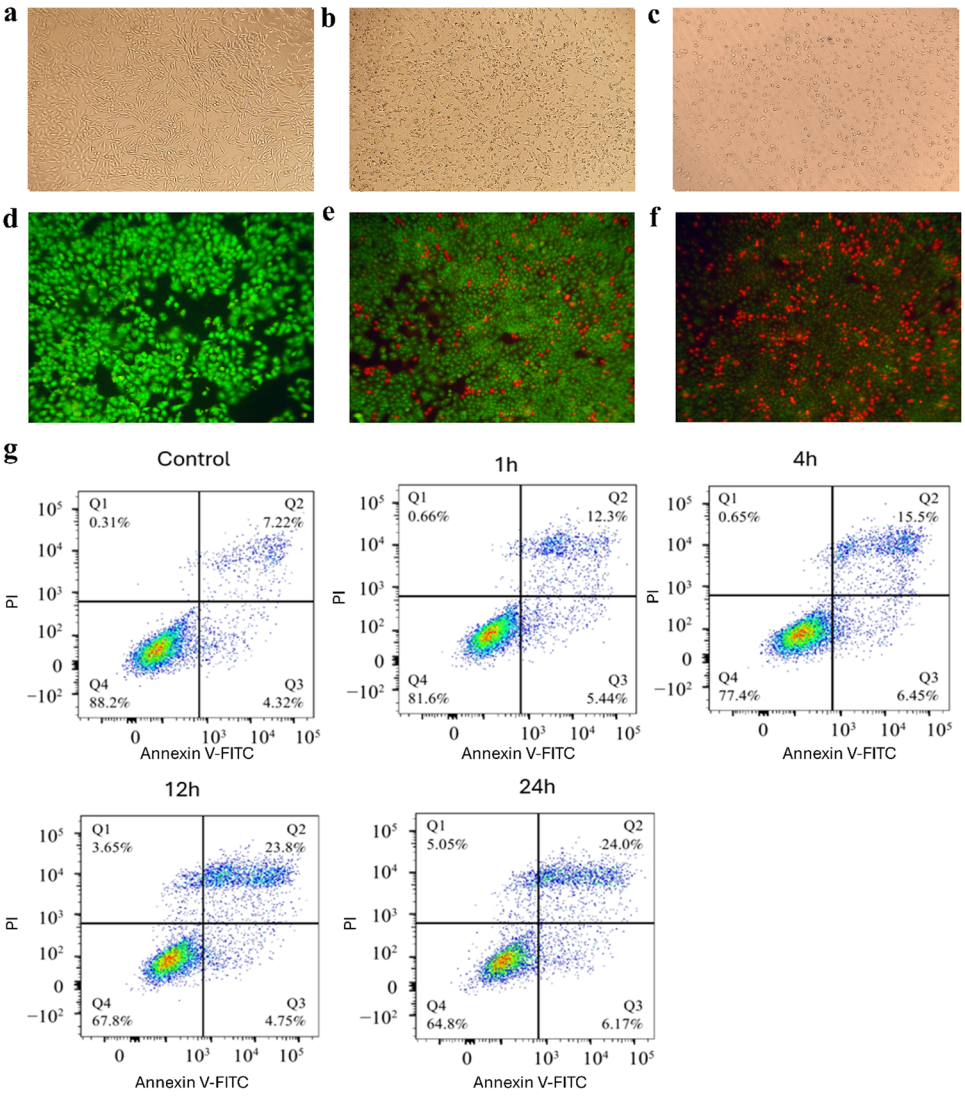

Figure 6. Phenotypic validation of time- and dose-dependent apoptotic responses induced by melittin in MDA-MB-231 cells. Phase-contrast micrographs show (a) untreated control cells with normal fibroblast-like morphology, (b) half IC_{50}-treated cells displaying mild cellular stress features and partial morphological alteration, and (c) IC_{50}-treated cells showing marked apoptotic collapse and loss of adherence. AO/EB dual fluorescence staining indicates (d) viable control cells, (e) early apoptotic features under half IC_{50} treatment, and (f) increased apoptotic and membrane-compromised cell populations under IC_{50} treatment. (g) Annexin V/PI flow cytometry quantitatively demonstrates a time- and dose-dependent increase in apoptotic cell populations following melittin exposure. These phenotypic findings support the DIA-PASEF proteomic trajectories observed across treatment conditions.

tional repression during cytotoxic stress rather than active stress signaling.[66] LRRC7 is a scaffold protein involved in cytoskeletal organization and cell−cell structural integrity, and its significant temporal downregulation indicates progressive structural disruption during melittin-induced cytotoxic stress rather than active regulation of stress signaling;[67] CPAMD8 is a poorly understood α2-macroglobulin−related protein that signals extensive cellular remodeling and disruption of homeostasis, rather than directly controlling mitochondrial quality-control pathways;[68] and SPATA4 is a stress-responsive protein that indicates progressive impairment of cellular homeostasis during cytotoxic remodeling and may contribute to apoptosis regulation.[69] Their simultaneous identification by both analytical layers supports their potential involvement in melittin-associated endoplasmic reticulum stress, mitochondrial dysfunction, and apoptosis-related remodeling. This consistency across different analytical methods supports their potential relevance as candidate temporal markers of the temporal progression of melittin's effects in TNBC cells.

3.3. Integrated Functional Interpretation of Time- and Dose-Dependent Proteomic Remodeling

The integrated analysis of Gene Ontology (GO), Kyoto Encyclopedia of Genes and Genomes (KEGG), and Reactome enrichment results reveals a clear, dose-dependent temporal structure in the proteomic response of MDA-MB-231 cells to melittin (Figure S2). Collectively, the exploratory multivariate patterns (Figure 3), differential-abundance trends (Figure 4), trajectory-based dynamics (Figure 5), and enrichment analyses (Tables S5−S10) indicate a pathway-level shift from early proteostatic adaptation toward progressive disruption of cellular homeostasis.

3.3.1. Early-Phase. At the half IC_{50} level, enrichment signatures are predominantly consistent with an adaptive response. GO terms related to translation, rRNA processing,

Downloaded from pubs.acs.org/jproobs/article-pdf/25/9/4704/6644586/acs.jproteome.6c00241.pdf by guest on 27 November 2026

https://doi.org/10.1021/acs.jproteome.6c00241
J. Proteome Res. 2026, 25, 4704−4718

ribosome biogenesis, regulation of protein metabolism, ubiquitin-dependent turnover, and vesicle-transport processes suggest activation of compensatory pathways that are likely to support proteostasis under mild stress (Table S5). This interpretation is supported by the modest early $\log_2$FC shifts and the close proximity of early half IC_{50} samples to controls in PCA space (Figure 3b).

In contrast, IC_{50} exposure is associated with broader early enrichment of pathways linked to RNA processing, spliceosome function, mRNA surveillance, ubiquitin-mediated proteolysis, aminoacyl-tRNA biosynthesis, and ribosomal components (Table S8), consistent with the stronger early separation observed in PCA (Figure 3a) and the higher-amplitude trajectory profiles (Figure 5a). Although canonical endoplasmic reticulum stress terms do not explicitly emerge at this stage, the combined proteostasis-related signatures are consistent with early accumulation of misprocessed RNA and an increased translational burden.

3.3.2. Mid-Phase. During the midphase, enrichment patterns suggest a transition from adaptive buffering toward progressive destabilization of RNA and protein networks. At half IC_{50}, terms linked to translation, RNA catabolism, chromatin remodeling, DNA metabolic processes, mitochondrial translation, and proteasomal regulation suggest that persistent stress begins to compromise biosynthetic and quality-control systems (Table S6). These pathway-level trends are consistent with intermediate trajectory behavior (Figure 5b) and the repositioning of midphase samples in PCA space (Figure 3b).

Under IC_{50}, midphase enrichment reveals substantially more extensive disruption. GO, KEGG, and Reactome terms highlight coordinated impairment across rRNA processing, RNA metabolism, mitochondrial and nuclear gene expression, chromatin organization, cell-cycle regulation, and global translation. The enrichment of spliceosome, RNA degradation, ribosome, and proteasome pathways further supports accelerated erosion of proteostasis during midphase IC_{50} exposure (Table S9).

3.3.3. Late-Phase. Late-phase responses further reinforce the dose-dependent divergence. At half IC_{50}, enrichment signatures are consistent with spliceosome dysfunction, mRNA surveillance, RNA degradation, proteasomal activation, impaired ribosome biogenesis, and nucleocytoplasmic transport defects (Table S7), alongside the emergence of autophagy-related terms, suggesting late-stage compensatory stress responses rather than dominant apoptotic signaling.

In contrast, late IC_{50} exposure shows the strongest and most comprehensive enrichment signatures in the data set. Pathways related to RNA metabolism, chromatin remodeling, mitochondrial gene expression, oxidative phosphorylation, ER protein processing, and extensive ubiquitin turnover are prominently represented (Table S10), consistent with the pronounced late-stage divergence observed in the heatmaps and trajectory profiles (Figure 5a). Together, these patterns suggest a deeply compromised cellular state.

3.3.4. Integrated Model. When interpreted alongside PCA positioning (Figure 3), differential-abundance patterns (Figure 4), and trajectory-based dynamics (Figure 5), the enrichment signatures support a dose-dependent continuum of melittin action. At half IC_{50}, the observed pathway-level signatures are consistent with an initially adaptive proteostasis program that gradually deteriorates as stress accumulates. By contrast, IC_{50} treatment is associated with coordinated enrichment patterns indicative of disrupted RNA maturation and translation, altered chromatin organization, mitochondrial dysfunction, and compromised protein-quality control, corresponding to a rapid shift toward a late-stage failure state. These findings collectively suggest that dose determines whether cells sustain transient compensation or progress toward advanced cellular dysfunction.

3.4. Integration of Proteomic Remodeling with Phenotypic Validation Supports Dose-Dependent Apoptotic Responses of Melittin

To determine whether the time- and dose-dependent molecular trajectories identified by DIA-PASEF reflect functional phenotypes, we performed phase-contrast imaging, AO/EB staining, and Annexin V/PI flow cytometry on MDA-MB-231 cells treated with melittin at half IC_{50} and IC_{50}. These assays provided independent validation that the proteomic signatures are consistent with a biological continuum from early adaptive stress to late apoptotic collapse. Phase-contrast microscopy revealed the earliest morphological differences between doses. Control cells (Figure 6a) exhibited normal fibroblast-like morphology, strong adhesion, intact cell−cell contacts, uniform nuclei, and high-density proliferation typical of a healthy, actively dividing TNBC culture. At half IC_{50} melittin (Figure 6b), most cells retained their structural integrity but showed subtle early stress features such as mild rounding, increased intercellular spacing, and occasional nuclear condensation, consistent with the proteomic evidence of active compensatory pathways, proteostasis maintenance, RNA processing, metabolic buffering, and mitochondrial support. In contrast, IC_{50} treatment (Figure 6c) caused pronounced apoptotic morphology, including extensive rounding and detachment, cytoplasmic contraction, loss of membrane definition, and membrane blebbing, features classically associated with apoptosis as previously reported.[69] These observations closely match the IC_{50} proteomic profile showing rapid disruption of ribosome biogenesis, spliceosomal function, endoplasmic reticulum stress, and mitochondrial dysfunction. AO/EB staining further differentiated apoptotic stages. Control cells showed uniform green fluorescence (Figure 6d), indicating intact membranes. At half IC_{50} exposure (Figure 6e), green cells still predominated, but there was an increase in yellow/orange fluorescence and chromatin condensation, characteristic of early apoptosis with partial membrane permeability and ionic imbalance. The IC_{50} treatment (Figure 6f) produced abundant orange/red emission, nuclear fragmentation, and extensive debris, signs of late apoptosis and secondary necrosis.[70] These findings support the proteomic observation that IC_{50} quickly overwhelms proteostasis and mitochondrial defenses, consistent with progression toward apoptotic cell death. Flow cytometry quantitatively confirmed these trajectories (Figure 6g). Control cells were mostly Annexin V^-/PI^-. Within 1 h of treatment, there was a small shift to Annexin V^+/PI^- early apoptosis, consistent with early mitochondrial outer-membrane disturbance and the early PCA separation. By 4 h, populations of Annexin V^+/PI^- and Annexin V^+/PI^+ increased sharply, indicating progression toward late apoptosis. At 12 h, the proportion of Annexin V-positive populations increased, indicating progression toward late apoptotic states and membrane-associated perturbations. By 24 h, IC_{50}-treated cells exhibited substantial apoptotic and morphological deterioration, including increased Annexin V-positive pop-

Downloaded from pubs.acs.org/jproobs/article-pdf/25/9/4704/6645868/acs.jproteome.6c00241.pdf by guest on 27 November 2026

https://doi.org/10.1021/acs.jproteome.6c00241
J. Proteome Res. 2026, 25, 4704−4718

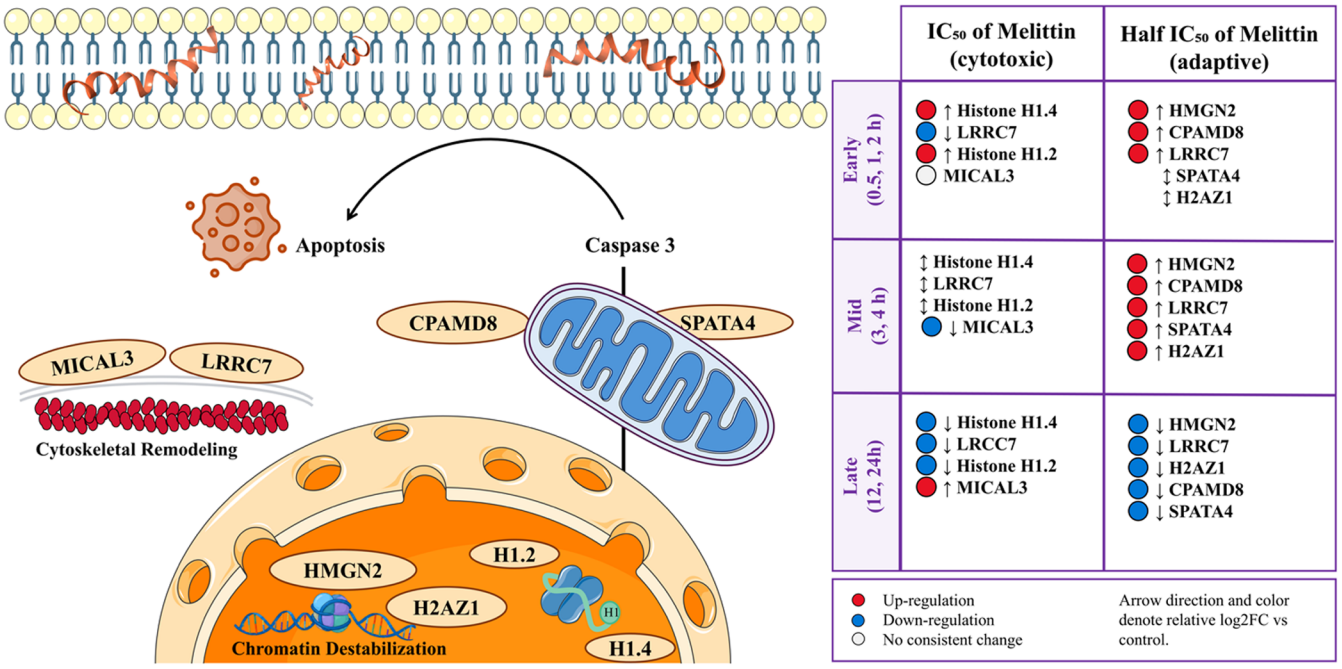

Figure 7. Schematic summary of time- and dose-dependent proteomic stress responses induced by melittin in MDA-MB-231 cells. Half IC_{50} treatment triggers a transient adaptive response characterized by stress tolerance and partial recovery, whereas IC_{50} treatment rapidly induces chromatin destabilization, RNA instability, cytoskeletal disruption and irreversible progression toward apoptotic commitment. Temporal progression is illustrated across early (0.5, 1, and 2 h), mid (3 and 4 h), and late (12 and 24 h) phases. Proteins included in the schematic were selected based on overlap between exploratory AUC-prioritized proteins and heatmap-defined high-magnitude temporal responders. Arrow direction and color denote relative $\log_2$ FC compared with untreated control. Red and blue symbols indicate relative up- and down-regulation, respectively, whereas white symbols denote proteins showing no consistent directional change across time points. The schematic summarizes inferred functional associations rather than direct molecular interactions.

ulations together with extensive apoptotic morphology observed by microscopy and AO/EB staining. Although a fraction of cells remained Annexin V^-/PI^- at this time point, these cells likely represented partially stressed or transitional populations that had not yet undergone complete membrane permeabilization at the time of analysis. Overall, these findings remain consistent with the severe late IC_{50} proteomic signatures associated with disruption of RNA processing, ribosomal function, mitochondrial homeostasis, and proteostasis networks. Microscopic, fluorescent, and flow-cytometric evidence collectively support the model suggested by the proteomics data. Half IC_{50} activates a controlled, adaptive stress response leading to delayed or reversible apoptosis, whereas IC_{50} was associated with rapid disruption across multiple cellular systems across transcriptional, translational, mitochondrial, and proteostasis networks, consistent with progression toward irreversible apoptotic execution. The temporal alignment between molecular and cellular findings strengthens the conclusion that melittin engages dose-dependent, time-resolved apoptotic pathways consistent with progression toward late-stage apoptotic dysfunction under IC_{50} exposure.

At half the IC_{50} exposure, the time-course trajectories of overlapping candidates suggest a mainly stress-tolerant response that develops gradually rather than undergoing abrupt cytotoxic deterioration. During the early window (0.5, 1, and 2 h), mild and temporary disruptions are seen across chromatin- and structure-related proteins, indicating that cellular architecture and nuclear organization mostly stay intact. HMGN2 (P05204) exhibits an early fluctuation instead of sustained activation, which aligns with short-term chromatin reorganization under manageable stress rather than stable transcription.[71−74] Meanwhile, H2A.Z (H2AZ1; P0C0S5) shows early sensitivity to melittin exposure, pointing to dynamic nucleosome remodeling without immediate major nuclear alteration.[75−77] As cells reach the midphase (3, 4 h), their adaptive buffering capacity begins to decline. The trends of HMGN2 and H2A.Z increasingly move downward, indicating a gradual reduction in chromatin accessibility and transcriptional capacity. Simultaneously, CPAMD8 (Q8IZJ3) and SPATA4 (Q8NEY3), two stress-sensitive proteins with poorly understood regulatory roles, remain persistently suppressed during this period, implying a general loss of cellular homeostasis rather than activation of a specific compensatory pathway.[78] LRRC7 (Q96NW7) shows temporal instability in this interval, suggesting that cellular architecture becomes more vulnerable as stress increases.[79] By the later phase (12, 24 h), half IC_{50} exposure leads to an apparent deterioration phenotype. Significant loss of chromatin-associated proteins (HMGN2 and H2A.Z) indicates late-stage chromatin destabilization and transcriptional shutdown. Simultaneously, strong downregulation of LRRC7 suggests a collapse of structural support and a loss of cytoskeletal anchoring. CPAMD8 and SPATA4 remain suppressed, supporting the idea that adaptive buffering has failed and that cells have shifted from delayed stress tolerance to a primed state with a slower, more gradual cytotoxic response. Notably, the absence of abrupt execution-phase signatures at this dose implies that cellular collapse occurs gradually rather than suddenly. In contrast, IC_{50} exposure triggers a rapid, irreversible process marked by early nuclear destabilization and subsequent structural remodeling. During the initial phase (0.5, 1, and 2 h), Histone

Downloaded from pubs.acs.org/jproteome/article-pdf/25/9/4704/6645868/acs.jproteome.6c00241.pdf by guest on 27 November 2026

https://doi.org/10.1021/acs.jproteome.6c00241
J. Proteome Res. 2026, 25, 4704−4718

H1.4 (P10412) and Histone H1.2 (P16403) undergo significant disruptions, indicating immediate changes in chromatin structure and nuclear organization.[80] This swift histone remodeling correlates with transcriptional stress and early chromatin breakdown under acute proteotoxic stress. Meanwhile, LRRC7 (Q96NW7) exhibits strong early suppression, suggesting a sudden loss of cytoskeletal and membrane-related structural integrity that exceeds the gradual changes observed at half IC_{50}. As cells reach the mid phase (3, 4 h), the proteomic landscape indicates a transition rather than recovery. Histone-related signals remain disrupted, showing that chromatin organization does not stabilize after the initial insult. LRRC7 exhibits, at most, limited and temporary changes without lasting recovery, aligning with a failed effort to maintain structural cohesion. Notably, MICAL3 (Q7RTP6) stays suppressed during this period, suggesting that large-scale actin remodeling has not yet begun and that cells remain in a pre-execution stress state.[81,82] During the late phase (12, 24 h), IC_{50}-treated cells undergo a fully committed cytotoxic process. Histone H1.4 and H1.2 show significant late depletion, indicating severe chromatin alteration and irreversible transcriptional shutdown. At the same time, a strong late induction of MICAL3 signals cytoskeletal remodeling during the execution phase, consistent with actin disassembly, membrane blebbing, and the final morphological changes observed phenotypically. Continuous suppression of LRRC7 further indicates the loss of cellular structure, collectively signaling the terminal failure of nuclear organization, structural integrity, and biosynthetic capacity.

Taken together, these trajectories define two fundamentally different stress responses caused by melittin. Half IC_{50} triggers a delayed and partially buffered response, where chromatin and structural damage gradually accumulate and only become fully evident at later times. In contrast, IC_{50} causes immediate nuclear collapse followed by later cytoskeletal remodeling, locking cells into a permanent, execution-phase state of cytotoxicity. This time-resolved mechanistic framework aligns well with the observed phenotypic progression and provides a clear molecular explanation for the dose-dependent divergence in melittin-induced cell death trajectories (Figure 7).

While the present study provides a detailed, time- and dose-resolved view of melittin-induced proteomic remodeling in TNBC cells, some limitations should be acknowledged. First, the analysis is inherently exploratory and relies on bottom-up, peptide-centric DIA proteomics, which does not allow unambiguous assignment of changes to specific protein isoforms or intact proteoforms. In addition, the lack of independent biological replicates precludes formal statistical inference, and effect-size–based metrics were therefore used to capture consistent temporal and dose-dependent trends. Despite these limitations, several factors support the consistency of the conclusions. The proteomic responses show strong internal coherence across multiple analytical layers, including PCA trajectories, differential-abundance patterns, trajectory-based AUC ranking, and pathway enrichment analyses, and they align well with previously reported mechanisms of melittin-induced stress and cytotoxicity. Importantly, the pathway-level consistency and the close agreement with independent phenotypic validation assays indicate that the observed trends reflect genuine biological processes rather than analytical noise. This integrated DIA-PASEF workflow provides a system-wide molecular snapshot of the cellular response to melittin within a single analytical framework and establishes a solid foundation for future hypothesis-driven studies, including targeted proteomics or functional validation of key regulatory nodes identified here.

4. CONCLUSION

This study provides a time- and dose-resolved proteomic framework for understanding how melittin influences cellular stress responses in MDA-MB-231 TNBC cells and distinguishes adaptive responses from progressive cytotoxic outcomes. By combining DIA-PASEF proteomics with trajectory-based protein prioritization and orthogonal phenotypic validation, our findings suggest that melittin induces hierarchically organized stress programs whose outcomes depend on both exposure level and treatment duration. Exposure to half-IC_{50} conditions was associated with a transient and partially compensatory response characterized by dynamic chromatin remodeling, RNA -associated buffering, and indirect mitochondrial quality-control signaling, which may contribute to the temporary maintenance of cellular homeostasis during early and midphases. In contrast, IC_{50} exposure was associated with more rapid disruption of these buffering systems, accompanied by early chromatin remodeling, RNA instability, and subsequent cytoskeletal disassembly, consistent with progression toward apoptotic cell death. The consistent temporal behavior of proteins such as LRRC7, histone variants, CPAMD8, SPATA4, and MICAL3 suggests that these proteins may serve as potential indicators of the transition from adaptive stress responses to late cytotoxic collapse. Together, these observations support a model in which melittin triggers a progressive and dose-dependent shift from adaptive stress signaling toward apoptotic dysfunction, rather than a uniform cytotoxic response. Because independent biological replicates were not available, formal statistical inference was not performed, and the proteomic findings should therefore be interpreted as exploratory and hypothesis-generating rather than confirmatory. Nevertheless, the consistency of temporal proteomic trajectories across doses, together with orthogonal validation by Annexin V/PI staining, AO/EB staining, and morphological observations, supports the biological relevance of the observed response patterns. This framework may help guide future investigations into dose selection strategies and proteomic features associated with adaptive versus irreversible responses in aggressive breast cancer models. Further studies incorporating independent biological replicates, additional TNBC cell lines, *in vivo* validation, and combination treatment settings will be necessary to confirm these observations and evaluate their broader translational relevance.

■ ASSOCIATED CONTENT

Data Availability Statement

The mass spectrometry proteomics data have been deposited to the ProteomeXchange Consortium via the MassIVE repository with the data set identifier PXD076669 and are publicly available at https://proteomecentral.proteomexchange.org/cgi/GetDataset?ID=PXD076669.

Supporting Information

The Supporting Information is available free of charge at https://pubs.acs.org/doi/10.1021/acs.jproteome.6c00241.

Schematic overview of the exploratory trajectory rank score calculation workflow; Log_2FC values relative to untreated controls were integrated across three biologically defined temporal windows: early (0.5, 1, and 2

Downloaded from pubs.acs.org/jproteome/article-pdf/25/9/4704/6645868/acs.jproteome.6c00241.pdf by guest on 27 November 2026

https://doi.org/10.1021/acs.jproteome.6c00241
J. Proteome Res. 2026, 25, 4704−4718

h), mid (3 and 4 h), and late (12 and 24 h); window-specific AUC values were calculated using trapezoidal integration based on the actual experimental time intervals; absolute AUC values were used to summarize the cumulative magnitude of temporal proteomic perturbation independently of regulation direction; the exploratory trajectory rank score was calculated as $|AUC_{early}| + 0.5|AUC_{mid}| + 0.5|AUC_{late}|$; reduced weighting of the mid- and late-phase components was applied as a descriptive heuristic to prioritize early temporal perturbation while still incorporating sustained later remodeling (Figure S1); a comparative summary of time- and dose-resolved pathway enrichment patterns following melittin treatment in MDA-MB-231 cells; the bubble plot summarizes representative GO, KEGG, and Reactome enrichment patterns across two melittin doses (half IC_{50} and IC_{50}) and three temporal windows: early (0.5, 1, and 2 h), mid (3 and 4 h), and late (12 and 24 h); pathways were selected based on their relevance to proteostasis, RNA metabolism, chromatin organization, mitochondrial function, and stress-response remodeling to illustrate the progressive transition from adaptive cellular stress responses toward widespread proteomic disruption under higher-dose exposure; bubble size represents the relative enrichment magnitude (intersection size of proteins associated with each pathway), whereas color intensity corresponds to enrichment significance expressed as $-\log_{10}$(FDR), with darker colors indicating higher statistical significance; the enrichment values were derived from the actual g:Profiler analyses were performed on differentially expressed proteins for each temporal window and treatment condition (Tables S5−S10); the figure is intended as a comparative summary visualization highlighting representative pathways associated with the temporal progression of melittin-induced proteomic remodeling (Figure S2) (PDF)

Summary of protein identifications and quantification metrics across all DIA-PASEF runs (Table S1); complete list of quantified proteins with log2 FC values for all time points and doses (Table S2); window-specific AUC metrics and exploratory trajectory ranking for half IC_{50} and IC_{50} treated proteins (Tables S3, S4); functional enrichment analysis results (GO, KEGG, Reactome) for early, mid, and late time windows at half IC_{50} and IC_{50} (Tables S5−S10); ranked proteins used for generation of the half IC_{50} and IC_{50} temporal trajectory heatmap, including normalized intensities, $\log_2$FC values at each time point, and cumulative absolute $\log_2$FC scores (Tables S11, S12) (XLSX)

AUTHOR INFORMATION

Corresponding Authors

Clizia Chinello − *University of Milano Bicocca, Department of Medicine and Surgery, Proteomics and Metabolomics Unit, Vedano al Lambro 20854, Italy*; orcid.org/0000-0002-7921-7768; Phone: +39-02-64488105; Email: clizia.chinello@unimib.it

Alireza Ghassempour − *Medicinal Plants and Drug Research Institute, Shahid Beheshti University, Tehran 1983969411, Iran*; Phone: +98-21-22431598; Email: a_ghassempour@yahoo.com

Authors

Farnaz Fatahian − *Medicinal Plants and Drug Research Institute, Shahid Beheshti University, Tehran 1983969411, Iran*; orcid.org/0009-0003-9167-5061

Seyed Mohammad Jafar Seyed Golestan − *Medicinal Plants and Drug Research Institute, Shahid Beheshti University, Tehran 1983969411, Iran*; orcid.org/0009-0007-3543-0894

Lisa Pagani − *University of Milano Bicocca, Department of Medicine and Surgery, Proteomics and Metabolomics Unit, Vedano al Lambro 20854, Italy*

Hassan Rezadoost − *Medicinal Plants and Drug Research Institute, Shahid Beheshti University, Tehran 1983969411, Iran*

Hossein Behboudi − *Medicinal Plants and Drug Research Institute, Shahid Beheshti University, Tehran 1983969411, Iran*; orcid.org/0000-0002-6613-3936

Andrew Smith − *University of Milano Bicocca, Department of Medicine and Surgery, Proteomics and Metabolomics Unit, Vedano al Lambro 20854, Italy*; orcid.org/0000-0001-6530-6113

Complete contact information is available at: https://pubs.acs.org/10.1021/acs.jproteome.6c00241

Author Contributions

[§]F.F. and S.M.J.G. contributed equally to this work, and A.G. and A.S. contributed equally as senior authors. Conceptualization, F.F., S.M.J.G., H.R., A.G., and A.S.; methodology, F.F., S.M.J.G., C.C., L.P., H.B., and A.S.; software, F.F., S.M.J.G., C.C., and L.P.; validation, F.F., S.M.J.G., C.C., and A.S.; formal analysis, F.F., S.M.J.G., and L.P; investigation, F.F., S.M.J.G., C.C., L.P., H.R., H.B., A.G., and A.S.; resources, A.G. and A.S.; data curation, F.F., S.M.J.G., and C.C.; writing original draft preparation, F.F., S.M.J.G., A.G., and A.S.; writing, review, and editing, F.F., S.M.J.G., C.C., L.P., H.R., H.B., A.G., and A.S.; visualization, F.F., S.M.J.G., C.C., L.P., H.R., H.B., A.G., and A.S.; supervision, A.G., A.S., and H.R.; project administration, A.S.; funding acquisition, A.S. All authors have read and agreed to the published version of the manuscript.

Funding

This work was supported by the National Plan for PNRR Complementary Investments (PNC, established with the decree-law 6 May 2021, no. 59, converted by law no. 101 of 2021) in the call for the funding of research initiatives for technologies and innovative trajectories in the healthcares sectors (Directorial Decree no. 931 of 06 − 06 − 2022) - project no. PNC0000003 - AdvaNced Technologies for Human-centrEd Medicine (project acronym: ANTHEM) and the Associazione Italiana Ricerca sul Cancro (AIRC), MFAG 2024 ID 31092.

Notes

This research did not involve human participants, animal subjects, or patient-derived materials; therefore, ethical approval and informed consent were not required, and the authors used ChatGPT (OpenAI) only to assist with language editing, grammar improvement, and refinement of the manuscript wording. All scientific content, data analyses, interpretations, and conclusions were developed, reviewed, and verified by the authors, who take full responsibility for the content of the manuscript.

The authors declare no competing financial interest.

Downloaded from pubs.acs.org/jproteome/article-pdf/25/9/4704/6645868/acs.jproteome.6c00241.pdf by guest on 27 November 2026

https://doi.org/10.1021/acs.jproteome.6c00241
J. Proteome Res. 2026, 25, 4704−4718

■ ACKNOWLEDGMENTS

F.F. gratefully acknowledges Shaghayegh Goodarzi for their invaluable assistance with sample preparation. The authors are deeply indebted to the University of Milano-Bicocca, Department of Medicine and Surgery (Metabolomics and Proteomics Unit), for hosting the research placement and providing access to laboratory facilities, instrumentation, and technical resources essential for this work. The support offered by Prof. A.S. in facilitating laboratory access, instrument time, and essential consumables during the collaborative period is sincerely appreciated.

■ REFERENCES

(1) Bray, F.; Laversanne, M.; Sung, H.; Ferlay, J.; Siegel, R. L.; Soerjomataram, I.; Jemal, A. Global Cancer Statistics 2022: GLOBOCAN Estimates of Incidence and Mortality Worldwide for 36 Cancers in 185 Countries. *Ca-Cancer J. Clin.* **2024**, *74* (3), 229−263.

(2) Kim, J.; Harper, A.; McCormack, V.; Sung, H.; Houssami, N.; Morgan, E.; Mutebi, M.; Garvey, G.; Soerjomataram, I.; Fidler-Benaoudia, M. M. Global Patterns and Trends in Breast Cancer Incidence and Mortality across 185 Countries. *Nat. Med.* **2025**, *31* (4), 1154−1162.

(3) Golestan, S. M. J. S.; Monza, N.; Fatahian, F.; Pagani, L.; AS'habi, M. A.; Behboudi, H.; Smith, A.; Ghassempour, A.; Denti, V. Sequential MALDI-MSI-Based Multiomics Reveals Spatial Lipid, Glycan, and Tryptic Peptide Signatures in Breast Tumor Histopathology. *Anal. Chem.* **2026**, *98* (19), 14503−14515.

(4) Freihat, O.; Sipos, D.; Kovacs, A. Global Burden and Projections of Breast Cancer Incidence and Mortality to 2050: A Comprehensive Analysis of GLOBOCAN Data. *Front. Public Health* **2025**, *13*, No. 1622954.

(5) Boyle, P. Triple-Negative Breast Cancer: Epidemiological Considerations and Recommendations. *Ann. Oncol* **2012**, *23* (6), vi7−vi12.

(6) Chen, Z.; Liu, Y.; Lyu, M.; Chan, C. H.; Sun, M.; Yang, X.; Qiao, S.; Chen, Z.; Yu, S.; Ren, M.; Lu, A.; Zhang, G.; Li, F.; Yu, Y. Classifications of Triple-Negative Breast Cancer: Insights and Current Therapeutic Approaches. *Cell Biosci.* **2025**, *15* (1), No. 13.

(7) Zagami, P.; Carey, L. A. Triple Negative Breast Cancer: Pitfalls and Progress. *NPJ. Breast Cancer* **2022**, *8* (1), No. 95.

(8) Yin, L.; Duan, J.-J.; Bian, X.-W.; Yu, S.-C. Triple-Negative Breast Cancer Molecular Subtyping and Treatment Progress. *Breast Cancer Res.* **2020**, *22* (1), No. 61.

(9) Sood, D.; Kaur, C.; Kumar, N.; Kumar, R.; Singh, G. Triple-Negative Breast Cancer: Challenges, Advances, and Promising Therapeutic Interventions. *Med. Oncol* **2025**, *42* (11), No. 506.

(10) Lehmann, B. D.; Bauer, J. A.; Chen, X.; Sanders, M. E.; Chakravarthy, A. B.; Shyr, Y.; Pietenpol, J. A. Identification of Human Triple-Negative Breast Cancer Subtypes and Preclinical Models for Selection of Targeted Therapies. *J. Clin. Invest* **2011**, *121* (7), 2750−2767.

(11) Li, Y.; Zhan, Z.; Yin, X.; Fu, S.; Deng, X. Targeted Therapeutic Strategies for Triple-Negative Breast Cancer. *Front. Oncol.* **2021**, *11*, No. 731535.

(12) Lebedeva, V.; Ebbinghaus, M.; Hidalgo, J. V.; Hardt, O.; Pfeifer, R. Triple-Negative Breast Cancer Unveiled: Bridging Science, Treatment Strategy, and Economic Aspects. *Int. J. Mol. Sci.* **2025**, *26* (19), No. 9714.

(13) Pajewska, M.; Partyka, O.; Czerw, A.; Deptała, A.; Sygit, K.; Gąska, I.; Porada, S.; Drobnik, J.; Pobrotyn, P.; Grata-Borkowska, U.; Furtak-Pobrotyn, J.; Banaś, T.; Małecki, K.; Grochans, E.; Grochans, S.; Cybulska, A. M.; Schneider-Matyka, D.; Bandurska, E.; Ciećko, W.; Czerw, N.; Marczak, M.; Sierocka, A.; Kozlowski, R. Advanced and Metastatic Triple Negative Breast Cancer—Potential New Treatment. *Cancers* **2025**, *17* (7), No. 1183.

(14) Chapman, M. P.; Risom, T.; Aswani, A. J.; Langer, E. M.; Sears, R. C.; Tomlin, C. J. Modeling Differentiation-State Transitions Linked to Therapeutic Escape in Triple-Negative Breast Cancer. *PLOS Comput. Biol.* **2019**, *15* (3), No. e1006840.

(15) Garg, P.; Singhal, G.; Horne, D.; Salgia, R.; Singhal, S. S. Metabolic Reprogramming in Breast Cancer: Pathways Driving Progression, Drug Resistance, and Emerging Therapeutics. *Biochim. Biophys. Acta, Rev. Cancer* **2025**, *1880* (5), No. 189396.

(16) Bai, X.; Ni, J.; Beretov, J.; Wasinger, V. C.; Wang, S.; Zhu, Y.; Graham, P.; Li, Y. Activation of the EIF2α/ATF4 Axis Drives Triple-Negative Breast Cancer Radioresistance by Promoting Glutathione Biosynthesis. *Redox Biol.* **2021**, *43* (10), No. 101993.

(17) Rizkallah, J.; Charbel, N.; Yassine, A.; El Masri, A.; Raffoul, C.; El Sardouk, O.; Ghezzawi, M.; Nasr, T. A.; Kreidieh, F. Melittin-Based Nanoparticles for Cancer Therapy: Mechanisms, Applications, and Future Perspectives. *Pharmaceutics* **2025**, *17* (8), No. 1019.

(18) Pandey, P.; Khan, F.; Khan, M. A.; Kumar, R.; Upadhyay, T. K. An Updated Review Summarizing the Anticancer Efficacy of Melittin from Bee Venom in Several Models of Human Cancers. *Nutrients* **2023**, *15* (14), No. 3111.

(19) Gajski, G.; Garaj-Vrhovac, V. Melittin: A Lytic Peptide with Anticancer Properties. *Environ. Toxicol. Pharmacol.* **2013**, *36* (2), 697−705.

(20) Prince, G.; Assi, A.; Aoude, M.; Kourie, H. R.; Haddad, F. Melittin, A Potential Game-Changer in the Fight Against Breast Cancer: A Systematic Review. *Anticancer Agents Med. Chem.* **2025**, *25* (15), 1077−1084.

(21) Li, X.; Zhu, S.; Li, Z.; Meng, Y.-Q.; Huang, S.-J.; Yu, Q.-Y.; Li, B. Melittin Induces Ferroptosis and ER Stress-CHOP-Mediated Apoptosis in A549 Cells. *Free Radical Res.* **2022**, *56* (5−6), 398−410.

(22) Li, X.; Li, Z.; Meng, Y.-Q.; Qiao, H.; Zhai, K.-R.; Li, Z.-Q.; Wei, S.-L.; Li, B. Melittin Kills A549 Cells by Targeting Mitochondria and Blocking Mitophagy Flux. *Redox Rep.* **2023**, *28* (1), No. 2284517.

(23) Roberto de Oliveira, M. Melittin-Induced Modulation of Mitochondrial Physiology: Beyond the Antitumoral Actions. *Toxicon* **2025**, *266*, No. 108555.

(24) Erkoc, P.; von Reumont, B. M.; Lüddecke, T.; Henke, M.; Ulshöfer, T.; Vilcinskas, A.; Fürst, R.; Schiffmann, S. The Pharmacological Potential of Novel Melittin Variants from the Honeybee and Solitary Bees against Inflammation and Cancer. *Toxins* **2022**, *14* (12), No. 818.

(25) Liu, J.; Xiao, S.; Li, J.; Yuan, B.; Yang, K.; Ma, Y. Molecular Details on the Intermediate States of Melittin Action on a Cell Membrane. *Biochim. Biophys. Acta* **2018**, *1860* (11), 2234−2241.

(26) Hong, J.; Lu, X.; Deng, Z.; Xiao, S.; Yuan, B.; Yang, K. How Melittin Inserts into Cell Membrane: Conformational Changes, Inter-Peptide Cooperation, and Disturbance on the Membrane. *Molecules* **2019**, *24* (9), No. 1775.

(27) Pratt, J. P.; Ravnic, D. J.; Huss, H. T.; Jiang, X.; Orozco, B. S.; Mentzer, S. J. Melittin-Induced Membrane Permeability: A Non-osmotic Mechanism of Cell Death. *In Vitro Cell. Dev. Biol. Anim.* **2005**, *41* (10), 349−355.

(28) Choi, K.; Hwang, C.; Gu, S.; Park, M.; Kim, J.; Park, J.; Ahn, Y.; Kim, J.; Song, M.; Song, H.; Han, S.-B.; Hong, J. Cancer Cell Growth Inhibitory Effect of Bee Venom via Increase of Death Receptor 3 Expression and Inactivation of NF-Kappa B in NSCLC Cells. *Toxins* **2014**, *6* (8), 2210−2228.

(29) Jeong, Y.-J.; Choi, Y.; Shin, J.-M.; Cho, H.-J.; Kang, J.-H.; Park, K.-K.; Choe, J.-Y.; Bae, Y.-S.; Han, S.-M.; Kim, C.-H.; Chang, H.-W.; Chang, Y.-C. Melittin Suppresses EGF-Induced Cell Motility and Invasion by Inhibiting PI3K/Akt/MTOR Signaling Pathway in Breast Cancer Cells. *Food Chem. Toxicol.* **2014**, *68*, 218−225.

(30) Jo, M.; Park, M. H.; Kollipara, P. S.; An, B. J.; Song, H. S.; Han, S. B.; Kim, J. H.; Song, M. J.; Hong, J. T. Anti-Cancer Effect of Bee Venom Toxin and Melittin in Ovarian Cancer Cells through Induction of Death Receptors and Inhibition of JAK2/STAT3 Pathway. *Toxicol. Appl. Pharmacol.* **2012**, *258* (1), 72−81.

(31) Moghaddam, F. D.; Akbarzadeh, I.; Marzbankia, E.; Farid, M.; Khaledi, L.; Reihani, A. H.; Javidfar, M.; Mortazavi, P. Delivery of

Downloaded from pubs.acs.org/jproteome/article-pdf/25/9/4704/6645868/acs.jproteome.6c00241.pdf by guest on 27 November 2026

https://doi.org/10.1021/acs.jproteome.6c00241
J. Proteome Res. 2026, 25, 4704−4718

Melittin-Loaded Niosomes for Breast Cancer Treatment: An in Vitro and in Vivo Evaluation of Anti-Cancer Effect. *Cancer Nanotechnol.* **2021**, *12* (1), No. 14.
(32) Kaya, B.; Sarigiannis, Y.; Nalbantsoy, A. Immunomodulatory Effects and Potential Therapeutic Application of Melittin in HER2-Expressing Breast Cancer Cells. *Int. J. Pept. Res. Ther.* **2025**, *31* (6), No. 110.
(33) Alibeigi, E.; Dehkordi, A. A.; Asadian, M.; Doosti, A.; Piri-Gharaghie, T. Administration of Apis Cerana Cerana Melittin Gene-Encapsulated Pectin for Breast Cancer Therapy: An Investigation of a New Anti-Cancer Agent. *Cancer Nanotechnol.* **2025**, *16* (1), No. 9.
(34) Daniluk, K.; Lange, A.; Wójcik, B.; Zawadzka, K.; Bałaban, J.; Kutwin, M.; Jaworski, S. Effect of Melittin Complexes with Graphene and Graphene Oxide on Triple-Negative Breast Cancer Tumors Grown on Chicken Embryo Chorioallantoic Membrane. *Int. J. Mol. Sci.* **2023**, *24* (9), No. 8388.
(35) Birhanu, A. G. Mass Spectrometry-Based Proteomics as an Emerging Tool in Clinical Laboratories. *Clin. Proteomics* **2023**, *20* (1), No. 32.
(36) Jimenez, C. R.; Verheul, H. M. W. Mass Spectrometry-Based Proteomics: From Cancer Biology to Protein Biomarkers, Drug Targets, and Clinical Applications. *Am. Soc. Clin. Oncol. Educ. Book* **2014**, No. 34, e504−e510.
(37) Tagliazucchi, L.; Costi, M. P. Mass Spectrometry Proteomics: A Key to Faster Drug Discovery. *J. Med. Chem.* **2025**, *69* (1), 30−71.
(38) Boys, E. L.; Liu, J.; Robinson, P. J.; Reddel, R. R. Clinical Applications of Mass Spectrometry-based Proteomics in Cancer: Where Are We? *Proteomics* **2023**, *23* (7−8), No. e2200238.
(39) Dowell, J. A.; Wright, L. J.; Armstrong, E. A.; Denu, J. M. Benchmarking Quantitative Performance in Label-Free Proteomics. *ACS Omega* **2021**, *6* (4), 2494−2504.
(40) Megger, D. A.; Bracht, T.; Meyer, H. E.; Sitek, B. Label-Free Quantification in Clinical Proteomics. *Biochim. Biophys. Acta, Proteins Proteomics* **2013**, *1834* (8), 1581−1590.
(41) Zhu, W.; Smith, J. W.; Huang, C.-M. Mass Spectrometry-Based Label-Free Quantitative Proteomics. *J. Biomed. Biotechnol.* **2010**, *2010* (1), No. 840518.
(42) Wang, J.; Tan, H.; Fu, Y.; Mishra, A.; Sun, H.; Wang, Z.; Wu, Z.; Wang, X.; Serrano, G. E.; Beach, T. G.; Peng, J.; High, A. A. Evaluation of Protein Identification and Quantification by the DiaPASEF Method on TimsTOF SCP. *J. Am. Soc. Mass Spectrom.* **2024**, *35* (6), 1253−1260.
(43) Panigrahi, A.; Hunt, A. L.; Assis, D.; Willetts, M.; Kallakury, B. V.; Davidson, B.; Ahn, J.; Conrads, T. P.; Goldman, R. Dia-PASEF Proteomics of Tumor and Stroma LMD Enriched from Archived HNSCC Samples. *ACS Omega* **2025**, *10* (13), 13296−13302.
(44) Skowronek, P.; Wallmann, G.; Wahle, M.; Willems, S.; Mann, M. An Accessible Workflow for High-Sensitivity Proteomics Using Parallel Accumulation−Serial Fragmentation (PASEF). *Nat. Protoc.* **2025**, *20* (6), 1700−1729.
(45) Savencu, O.; Liscu, H.-D.; Verga, N. Systems Theory in Oncology: A Narrative Review of an Integrative Framework for Understanding Cancer Complexity. *Physiologia* **2025**, *5* (4), No. 48.
(46) Rosati, D.; Palmieri, M.; Brunelli, G.; Morrione, A.; Iannelli, F.; Frullanti, E.; Giordano, A. Differential Gene Expression Analysis Pipelines and Bioinformatic Tools for the Identification of Specific Biomarkers: A Review. *Comput. Struct. Biotechnol. J.* **2024**, *23*, 1154−1168.
(47) Mosca, E.; Alfieri, R.; Merelli, I.; Viti, F.; Calabria, A.; Milanesi, L. A Multilevel Data Integration Resource for Breast Cancer Study. *BMC Syst. Biol.* **2010**, *4* (1), No. 76.
(48) Mobashir, M.; Turunen, S. P.; Izhari, M. A.; Ashankyty, I. M.; Helleday, T.; Lehti, K. An Approach for Systems-Level Understanding of Prostate Cancer from High-Throughput Data Integration to Pathway Modeling and Simulation. *Cells* **2022**, *11* (24), No. 4121.
(49) Djomehri, S. I.; Gonzalez, M. E.; da Veiga Leprevost, F.; Tekula, S. R.; Chang, H.-Y.; White, M. J.; Cimino-Mathews, A.; Burman, B.; Basrur, V.; Argani, P.; Nesvizhskii, A. I.; Kleer, C. G. Quantitative Proteomic Landscape of Metaplastic Breast Carcinoma Pathological Subtypes and Their Relationship to Triple-Negative Tumors. *Nat. Commun.* **2020**, *11* (1), No. 1723.
(50) Escobar-Hoyos, L.; Knorr, K.; Abdel-Wahab, O. Aberrant RNA Splicing in Cancer. *Annu. Rev. Cancer Biol.* **2019**, *3* (1), 167−185.
(51) Wang, B.-D.; Lee, N. Aberrant RNA Splicing in Cancer and Drug Resistance. *Cancers* **2018**, *10* (11), No. 458.
(52) Furlan, C.; Suarez-Diez, M.; Saccenti, E. A Validated Proteomic Signature of Basal-like Triple-Negative Breast Cancer Subtypes Obtained from Publicly Available Data. *Cancers* **2025**, *17* (16), No. 2601.
(53) Xu, W.; Dong, L.; Dai, J.; Zhong, L.; Ouyang, X.; Li, J.; Feng, G.; Wang, H.; Liu, X.; Zhou, L.; Xia, Q. The Interconnective Role of the UPS and Autophagy in the Quality Control of Cancer Mitochondria. *Cell. Mol. Life Sci.* **2025**, *82* (1), No. 42.
(54) Fatahian, F.; Rezadoost, H.; Golestan, S. M. J. S.; Behboudi, H.; Catani, M.; Cavazzini, A.; Ghassempour, A. Analytical Characterization and Stability Evaluation of High-Purity Melittin Isolated from Crude Bee Venom via One-Step, Scalable Reversed-Phase Liquid Chromatography. *J. Chromatogr. A* **2026**, *1766*, No. 466605.
(55) Stella, M.; Chinello, C.; Cazzaniga, A.; Smith, A.; Galli, M.; Piga, I.; Grasso, A.; Grasso, M.; Del Puppo, M.; Varallo, M.; Bovo, G.; Magni, F. Histology-Guided Proteomic Analysis to Investigate the Molecular Profiles of Clear Cell Renal Cell Carcinoma Grades. *J. Proteomics* **2019**, *191*, 38−47.
(56) Previtali, P.; Pagani, L.; Risca, G.; Capitoli, G.; Bossi, E.; Oliveira, G.; Piga, I.; Radice, A.; Trezzi, B.; Sinico, R. A.; Magni, F.; Chinello, C. Towards the Definition of the Molecular Hallmarks of Idiopathic Membranous Nephropathy in Serum Proteome: A DIA-PASEF Approach. *Int. J. Mol. Sci.* **2023**, *24* (14), No. 11756.
(57) Saettini, F.; Guerra, F.; Mauri, M.; Salter, C. G.; Adam, M. P.; Adams, D.; Baple, E. L.; Barredo, E.; Bhatia, S.; Borkhardt, A.; Brusco, A.; Bugarin, C.; Chinello, C.; Crosby, A. H.; D'Souza, P.; Denti, V.; Fazio, G.; Giuliani, S.; Kuehn, H. S.; Amel, H.; Elmi, A.; Lo, B.; Malighetti, F.; Mandrile, G.; Martín-Nalda, A.; Mefford, H. C.; Moratto, D.; Emam Mousavi, F.; Nelson, Z.; Gutiérrez-Solana, L. G.; Macnamara, E.; Michaud, V.; O'Leary, M.; Pagani, L.; Pavinato, L.; Santamaria, P. Vv.; Planas-Serra, L.; Quadri, M.; Raspall-Chaure, M.; Rebellato, S.; Rosenzweig, S. D.; Roubertie, A.; Holzinger, D.; Deal, C.; Vockley, C. W.; Savino, A. M.; L Stoddard, J.; Uhlig, H. H.; Pujol, A.; Magni, F.; Paglia, G.; Cazzaniga, G.; Piazza, R.; Barberis, M.; Biondi, A. Biallelic PI4KA Mutations Disrupt B-Cell Metabolism and Cause B-Cell Lymphopenia and Hypogammaglobulinemia. *J. Clin. Immunol.* **2025**, *45* (1), No. 15.
(58) Feng, J.; Meyer, C. A.; Wang, Q.; Liu, J. S.; Shirley Liu, X.; Zhang, Y. GFOLD: A Generalized Fold Change for Ranking Differentially Expressed Genes from RNA-Seq Data. *Bioinformatics* **2012**, *28* (21), 2782−2788.
(59) Li, Q.; Roxas, B. A. An Assessment of False Discovery Rates and Statistical Significance in Label-Free Quantitative Proteomics with Combined Filters. *BMC Bioinf.* **2009**, *10* (1), No. 43.
(60) Nimer, R. M.; Alfaqih, M. A.; Shehabat, E. R.; Mujammami, M.; Rahman, A. M. A. Label-Free Quantitative Proteomics Analysis for Type 2 Diabetes Mellitus Early Diagnostic Marker Discovery Using Data-Independent Acquisition Mass Spectrometry (DIA-MS). *Sci. Rep.* **2023**, *13* (1), No. 20880.
(61) Pruessner, J. C.; Kirschbaum, C.; Meinlschmid, G.; Hellhammer, D. H. Two Formulas for Computation of the Area under the Curve Represent Measures of Total Hormone Concentration versus Time-Dependent Change. *Psychoneuroendocrinology* **2003**, *28* (7), 916−931.
(62) Bossy-Wetzel, E.; Green, D. R. Detection of Apoptosis by Annexin V Labeling. *Methods Enzymol.* **2000**, *322*, 15−18.
(63) Duffy, C.; Sorolla, A.; Wang, E.; Golden, E.; Woodward, E.; Davern, K.; Ho, D.; Johnstone, E.; Pfleger, K.; Redfern, A.; Iyer, K. S.; Baer, B.; Blancafort, P. Honeybee Venom and Melittin Suppress Growth Factor Receptor Activation in HER2-Enriched and Triple-Negative Breast Cancer. *NPJ. Precis. Oncol.* **2020**, *4* (1), No. 24.
(64) Dubey, S. K.; Dubey, R.; Kleinman, M. E. Unraveling Histone Loss in Aging and Senescence. *Cells* **2024**, *13* (4), No. 320.

Downloaded from pubs.acs.org/jproobs/article-pdf/25/9/4704/6645868/acs.jproteome.6c00241.pdf by guest on 27 November 2026

https://doi.org/10.1021/acs.jproteome.6c00241
J. Proteome Res. 2026, 25, 4704−4718

(65) Lai, S.; Jia, J.; Cao, X.; Zhou, P.-K.; Gao, S. Molecular and Cellular Functions of the Linker Histone H1.2. *Front. Cell Dev. Biol.* **2022**, *9*, No. 773195.
(66) Zhang, S.; Postnikov, Y.; Lobanov, A.; Furusawa, T.; Deng, T.; Bustin, M. H3K27ac Nucleosomes Facilitate HMGN Localization at Regulatory Sites to Modulate Chromatin Binding of Transcription Factors. *Commun. Biol.* **2022**, *5* (1), No. 159.
(67) Willim, J.; Woike, D.; Greene, D.; Das, S.; Pfeifer, K.; Yuan, W.; Lindsey, A.; Itani, O.; Böhme, A. L.; Tibbe, D.; Hönck, H.-H.; Hassani Nia, F.; Zech, M.; Brunet, T.; Faivre, L.; Sorlin, A.; Vitobello, A.; Smol, T.; Colson, C.; Baranano, K.; Schatz, K.; Bayat, A.; Schoch, K.; Spillmann, R.; Davis, E. E.; Conboy, E.; Vetrini, F.; Platzer, K.; Neuser, S.; Gburek-Augustat, J.; Grace, A. N.; Mitchell, B.; Stegmann, A.; Sinnema, M.; Meeks, N.; Saunders, C.; Cadieux-Dion, M.; Hoyer, J.; Van-Gils, J.; de Sainte-Agathe, J.-M.; Thompson, M. L.; Bebin, E. M.; Weisz-Hubshman, M.; Tabet, A.-C.; Verloes, A.; Levy, J.; Latypova, X.; Harder, S.; Silverman, G. A.; Pak, S. C.; Schedl, T.; Freson, K.; Mumford, A.; Turro, E.; Schlein, C.; Shashi, V.; Kreienkamp, H.-J. Variants in LRRC7 Lead to Intellectual Disability, Autism, Aggression and Abnormal Eating Behaviors. *Nat. Commun.* **2024**, *15* (1), No. 7909.
(68) Li, Z.-F.; Wu, X.; Engvall, E. Identification and Characterization of CPAMD8, a Novel Member of the Complement 3/α 2 -Macroglobulin Family with a C-Terminal Kazal Domain. *Genomics* **2004**, *83* (6), 1083−1093.
(69) Wei, R.; Xu, L. W.; Liu, J.; Li, Y.; Zhang, P.; Shan, B.; Lu, X.; Qian, L.; Wu, Z.; Dong, K.; Zhu, H.; Pan, L.; Yuan, J.; Pan, H. SPATA2 Regulates the Activation of RIPK1 by Modulating Linear Ubiquitination. *Genes Dev.* **2017**, *31* (11), 1162−1176.
(70) Alabsi, A. M.; Ali, R.; Ali, A. M.; Al-Dubai, S. A. R.; Harun, H.; Kasim, N. H. A.; Alsalahi, A. Apoptosis Induction, Cell Cycle Arrest and in Vitro Anticancer Activity of Gonothalamin in a Cancer Cell Lines. *Asian Pac. J. Cancer Prev.* **2012**, *13* (10), 5131−5136.
(71) Craig, J. M.; Turner, T. H.; Harrell, J. C.; Clevenger, C. V. Prolactin Drives a Dynamic STAT5A/HDAC6/HMGN2 Cis-Regulatory Landscape Exploitable in ER+ Breast Cancer. *Endocrinology* **2021**, *162* (5), No. bqab036.
(72) Murphy, K. J.; Cutter, A. R.; Fang, H.; Postnikov, Y. V.; Bustin, M.; Hayes, J. J. HMGN1 and 2 Remodel Core and Linker Histone Tail Domains within Chromatin. *Nucleic Acids Res.* **2017**, *45* (17), 9917−9930.
(73) Schauwecker, S. M.; Kim, J. J.; Licht, J. D.; Clevenger, C. V. Histone H1 and Chromosomal Protein HMGN2 Regulate Prolactin-Induced STAT5 Transcription Factor Recruitment and Function in Breast Cancer Cells. *J. Biol. Chem.* **2017**, *292* (6), 2237−2254.
(74) Medler, T. R.; Craig, J. M.; Fiorillo, A. A.; Feeney, Y. B.; Harrell, J. C.; Clevenger, C. V. HDAC6 Deacetylates HMGN2 to Regulate Stat5a Activity and Breast Cancer Growth. *Mol. Cancer Res.* **2016**, *14* (10), 994−1008.
(75) Li, S.; Wei, T.; Panchenko, A. R. Histone Variant H2A.Z Modulates Nucleosome Dynamics to Promote DNA Accessibility. *Nat. Commun.* **2023**, *14* (1), No. 769.
(76) Sales-Gil, R.; Kommer, D. C.; de Castro, I. J.; Amin, H. A.; Vinciotti, V.; Sisu, C.; Vagnarelli, P. Non-Redundant Functions of H2A.Z.1 and H2A.Z.2 in Chromosome Segregation and Cell Cycle Progression. *EMBO Rep.* **2021**, *22* (11), No. e52061.
(77) Rangasamy, D. Histone Variant H2A.Z Can Serve as a New Target for Breast Cancer Therapy. *Curr. Med. Chem.* **2010**, *17* (28), 3155−3161.
(78) Jiang, J.; Li, L.; Xie, M.; Fuji, R.; Liu, S.; Yin, X.; Li, G.; Wang, Z. SPATA4 Counteracts Etoposide-Induced Apoptosis via Modulating Bcl-2 Family Proteins in HeLa Cells. *Biol. Pharm. Bull.* **2015**, *38* (10), 1458−1463.
(79) Lassila, M.; Juhila, J.; Heikkilä, E.; Holthöfer, H. Densin Is a Novel Cell Membrane Protein of Sertoli Cells in the Testis. *Mol. Reprod. Dev.* **2007**, *74* (5), 641−645.
(80) Hergeth, S. P.; Schneider, R. The H1 Linker Histones: Multifunctional Proteins beyond the Nucleosomal Core Particle. *EMBO Rep.* **2015**, *16* (11), 1439−1453.
(81) Liu, Q.; Liu, F.; Yu, K. L.; Tas, R.; Grigoriev, I.; Remmelzwaal, S.; Serra-Marques, A.; Kapitein, L. C.; Heck, A. J. R.; Akhmanova, A. MICAL3 Flavoprotein Monooxygenase Forms a Complex with Centralspindlin and Regulates Cytokinesis. *J. Biol. Chem.* **2016**, *291* (39), 20617−20629.
(82) Tominaga, K.; Minato, H.; Murayama, T.; Sasahara, A.; Nishimura, T.; Kiyokawa, E.; Kanauchi, H.; Shimizu, S.; Sato, A.; Nishioka, K.; Tsuji, E.; Yano, M.; Ogawa, T.; Ishii, H.; Mori, M.; Akashi, K.; Okamoto, K.; Tanabe, M.; Tada, K.; Tojo, A.; Gotoh, N. Semaphorin Signaling via MICAL3 Induces Symmetric Cell Division to Expand Breast Cancer Stem-like Cells. *Proc. Natl. Acad. Sci. U.S.A.* **2019**, *116* (2), 625−630.

Downloaded from pubs.acs.org/jproteome/article-pdf/25/9/4704/6445868/acs.jproteome.6c00241.pdf by guest on 27 November 2026

https://doi.org/10.1021/acs.jproteome.6c00241
J. Proteome Res. 2026, 25, 4704−4718